Alma Mater Studiorum · University of Bologna

School of Science
Department of Physics and Astronomy
Master Degree in Physics

Development of an impedance based biosensor for studies of spheroids formation

Supervisor:
Prof.ssa Beatrice Fraboni

Co-supervisor:
Prof. Schönherr
Dr. Francesco Decataldo
Dr. Isabella Zironi

Submitted by:
Cristiana Antonella Mastropierro

Academic Year 2021/2022

Contents

Abstract

Three-dimensional (3D) multicellular spheroids are exceptional *in vitro* cell models for their ability to accurately mimic real cell-cell interaction processes. However, the challenges in producing well-defined spheroids with controlled size together with the deficiency of techniques to monitor them significantly restrict their use. Herein, a novel device to study spheroid formation in real time is presented. By exploiting electrochemical impedance spectroscopy, a multi-electrode array (MEA) attached to a calcium alginate scaffold is able to monitor the behaviour of 36 different hydrogel wells. The scaffold contains inverted shape pyramidal microwells, which guide the aggregation of cells into spheroids with controlled dimensions. Preliminar studies on calcium alginate, optimisation of fabrication strategy are shown, together with testing of the device in the presence and the absence of the hydrogel. Lastly, the device was tested for its intended aim, i.e. to monitor the formation of a spheroid, proving its potential as an impedance biosensor.

Part I

Introduction to the problem and methods

Chapter 1

State of the art

In vitro models are a well-established methodology to study a variety of problems not only in biology, but also and even more in medical fields, such as drug permeability or delivery and cancer studies. Such cell models are mainly composed of immortalized cells growing in spread-out cell submonolayers or confluent monolayers on permeable substrates, depending on cell type and culture conditions: this standard configuration is defined as two-dimensional (2D) cell culture. During many biological processes, cell-cell interactions, communications and contacts are crucial for cellular functions and regulation of proper signal pathways[1]. As a consequence, when cells are cultured in a not native environment, i.e. cultured in vitro, many information can be lost. The ability to reintroduce such interactions is, therefore, fundamental for preserving cellular viability and phenotype and can lead to advances in many fields, from cell biology to tissue engineering. Three-dimensional (3D) cell culture models take into the account this problem: when cultured on non-adherent substrates, cells tend to self-organise in stable 3D structures, known as spheroids or organoids, sharing the same extracellular matrix. Compared to traditional 2D cell culture, multi-cellular spheroids are proven to better mimic the real physiological environment[2], renewing attention and hope in the feasibility of maturing 3D systems for therapy test platforms with greater power to predict clinical efficacy.
Despite the great increase in the use of spheroids in the last decade, there is a still a gap regarding the technologies available for monitoring them. Moreover, procedure currently considered as gold standards, such as end-point histology or fluorescence microscopy, require the destruction of the tissue for sampling and staining or have limited lifespan, being not suitable for continuous 3D culture monitoring[3]. Label free electrochemical impedance sensors has been proven to be a proficient methods for sensing many biological processes and parameters[4–6], with the advantages of being non-invasive and being relatively non-expensive. With impedance measurements, cell growth, activity, and changes in cell composition, shape or location can be sensed[7],but, to date, these have been mainly used for 2D cultures[8, 9].

Among different impedance measurements, we can distinguish between three major techniques: electric cell-substrate impedance sensing (ECIS), impedance flow cytometry (IFC) and electrochemical impedance spectroscopy (EIS) [10]. ECIS is used to monitor adherent cells as they grow on electrodes. In such way, any biological process associated with cell morphology or membrane impedance can be evaluated measuring the cellular impedance. IFC is, instead, suited for suspended cells flowing through microfluidic channels. It is mostly used to analyse massive number of cells, such as in blood anlysis, and detection.
Finally, we can find different examples of EIS used to monitor 3D cell culture[11, 12] and in particular cells proliferation within spheroids has been successfully achieved using this technique[13, 14].
This chapter will focus on EIS for 3D cell culture and materials commonly used for such bioelectronic applications.

1.1 Impedance spectroscopy based sensors for three dimensional cell culture studies

Electrochemical impedance spectroscopy is a powerful technique able to investigate cell status, exploiting variations in current/voltage through the cells, either suspended or adherent. Owing to the use of a low voltage frequency-dependent AC signal sweeping, it is considered an almost steady-state analysis[10]. Thus, it is possible to probe over a wide frequency range, from less than 1 mHz to more than 1 MHz, using commercially available electrochemical working stations (potentiostat). Sweeping frequency allows EIS to provide richer information in real time, without affecting cells behaviour.
An impedance based sensor is typically a passive system: in order to convert an external event into a measurable signal, a stimulation source injects energy (either a voltage or a current) into the sensor, which reflects such event in its impedance variation [15]. Commonly, the setup consists in an electrochemical cell with three electrodes, a working electrode (WE), a counter electrode (CE) and a reference electrode (RE), exploiting a defined equivalent model to obtain the information required, as better explained further.

1.1.1 Basic principles of EIS

The impedance of a system is typically measured applying a voltage perturbation, usually sinusoidal, to a working electrode and collecting the resulting current wave. The impedance Z is so defined as the ratio between the time dependent voltage function $V(t)$ and the current response $I(t)$ at each frequency f, :

$$Z = \frac{V(t)}{I(t)} = \frac{V_0 \cdot \sin(2\pi f t)}{I_0 \cdot \sin(2\pi f t + \phi)} \tag{1.1}$$

where V_0 and I_0 are the maximum voltage and current signals and t the time. The response $I(t)$ is pseudo linear, so that a phase shift ϕ is added to the sinusoidal response. It is a complex value, in which the real part Z_r is usually associated to the resistive behaviour and does not depend on frequency and the imaginary part Z_i is frequency-dependent and related to a more capacitive behaviour. Thus, the impedance can be described by the modulus $|Z|$ and the phase shift or the two real and imaginary components, which are all related by:

$$Z = Z_r + iZ_i(2\pi f) \qquad |Z| = \sqrt{Z_r^2 + Z_i^2(2\pi f)} \qquad \phi = \tan^{-1}(\frac{Z_i}{Z_r}) \tag{1.2}$$

These can be directly derived from the Nyquist plot of impedance values in Fig.1.1(a), in which Z_r is plotted on the X-axis and Z_i is plotted on the Y-axis, so that impedance can also be seen as the vector of length $|Z|$. It is often used also the Cole-Cole plot (Fig.1.1(b)), which is a type of Nyquist plot, where the X-axis plots the real part and the Y-axis the negative imaginary part. The Cole-Cole diagram offers the advantage to clearly show time constants corresponding to semicircles in the plane[16]. Another common illustration is the Bode plot, in Fig1.1(c), that comprises two separate logarithmic plots: $|Z|$ versus frequency and/or phase vs frequency.

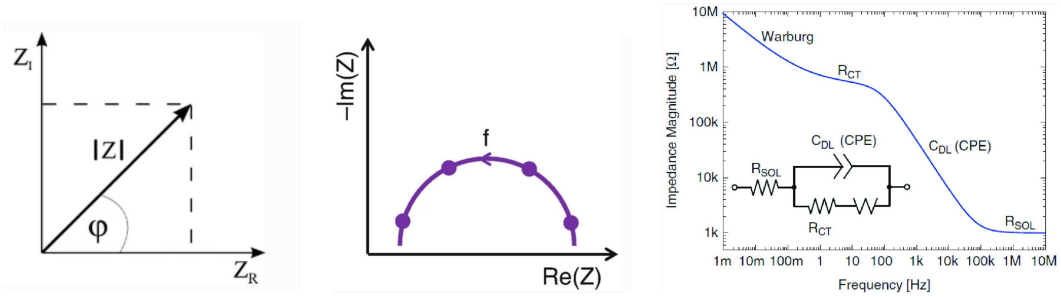

(a) **(b)** **(c)**

Figure 1.1: Three examples of impedance results representation: (a)[17] a Nyquist example plot; (b)[17] a Cole-Clot example plot; (c)[16] a Bode example plot with the corresponding equivalent Randles model, showing Faradic (R_{CT}) and non Faradaic (C_{DL}) phenomena.

What is also reported in Fig.1.1(c) is the Randles model of the system under analysis, i.e. a circuit in which each element of the system is represented by either a capacitor, resistance or constant phase element. Indeed, the electrochemical interface, drawn in Fig.1.2, extremely relevant in biosensing, is described by the following components. The double layer due to non-Faradic interaction between the electrode and the electrolyte is modeled as a capacitance C_{DL}, since at this boundary a layer of electrons on the electrode and a layer of opposite charge in the solution are created and separated by a single layer of solvent molecules acting as a dielectric. Its value depends on the electrode area, the ion concentration and on the bias voltage. Roughness, porosity or non-homogeneity of

the electrode can lead to a global pseudo-capacitive behaviour, which is consider using a constant phase element in place of the capacitor; since this term is usually small for reasonably smooth electrodes, it could be usually neglected, approximating the element with an ideal capacitor. The ionic buffer has a bulk conductivity, expressed by R_{SOL}, that in modern micrometric electrodes is only influenced by the perimeter of the working electrode, and it is connected in series to the double-layer capacitance.

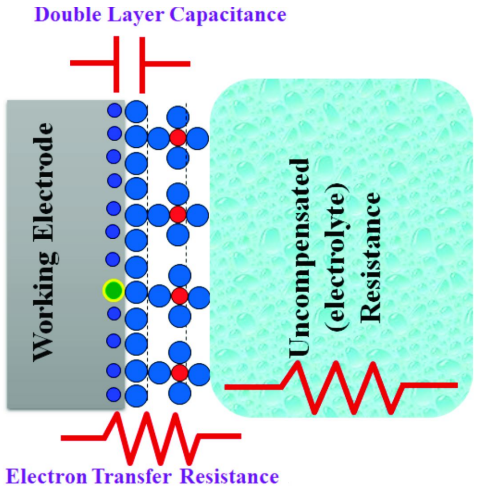

Figure 1.2: A simple scheme to describe EIS circuit and the redox reaction that takes place at the interface between the working electrode and the electrolyte, from [18].

In the same way, also the concentration of electroactive species, charge-transfer, and mass-transfer from the bulk solution to the electrode surface (shown through interactions at the interface) can be characterised by electrical components in series or parallel. So, a Faradic branch containing such components is connected in parallel to C_{DL}. The first term is the charge transfer resistance (R_{CT}), that is the difficulty of the charge exchange between the ionic solution and the electrode. In series to it, a Warburg impedance (W) takes in account for diffusion processes of redox species at the electrode-electrolyte interface.
The values of the model parameters are often fitted from experimental data, studying the Nyquist shape. Therefore, the EIS curve is the most important datum to be obtained first, and then surface characteristics are evaluated from fitting the electrical circuit.

1.1.2 Cellular model in the EIS

The presence of a cell on top of a planar electrode can be simulated as shown in Fig.1.3, using the widely accepted *single-shell model*. The cell corresponds to a capacitance C_M, usually of ∼0.01 pF/ μm^2 for the membrane with thickness of about 4 nm, as deemed for the typical cell size range between 10 and 100 μm, in series with the cytoplasm impedance ($R_C||C_C$)[15]. Consequently, the cell can be viewed as a conducting sphere with conductivity similar to the culture medium (around 1.5 S/m) and an insulating thin shell, until operating frequencies that shunts C_M (usually below 100 kHz). So as a cell approaches the electric field established between the sensing electrodes, the contrast in conductivity with the electrolyte displaced causes an increase of the solution resistance measured. Then, the adhesion of a cell on the electrode surface alter also R_{SOL} and C_{DL}. The first increases because the insulating barrier given by the presence of the cell reduces conductive paths for solution ions. At the same way, ion forming the double layer are displaced by the cell and so the impedance reduces. Thus, all those effects result in an

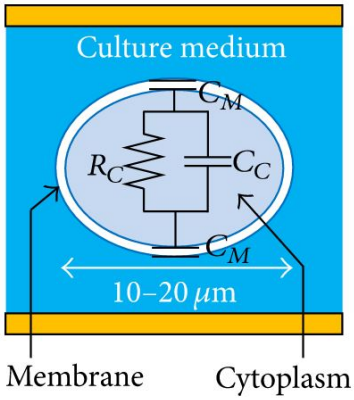

Figure 1.3: Electrical equivalent of a cell, from [15].

increase of the impedance spectrum and this continues during adhesion and duplication of cells until the colony reaches confluence. When some cells die for lack of nutrients or due to some external interventions, like in drug or radiation effects studies, they start to detach and hence the impedance starts to decrease.
Another model worth mentioning is the so-called *double-shell model*, that might be used for plants, yeast or bacteria cells. It takes into account the presence of external matrices outside the plasma membrane (a second insulating wall); it can be deduced from the single-shell model, as well discussed in Ref [19].

1.1.3 Impedance measurements in 3D cell culture

By means of impedance sensing, it is thus possible to monitor the culture growth in real time, mainly relying on the adhesion or proximity of cells to the electrode. This does not occur for 3D cell culture as they contain complex matrices, polymer scaffolds, or discrete suspended cell clusters. EIS must then be adapted by ensuring sensitivity of the sensor or sensor array to cell suspended or in a scaffold, by preserving an even electronic field in the whole system, and by being suitable for the different culture format.
The design and integration of electrodes inside a 3D culture is one of the most important challenges, due to the stiffness of the materials and the need for a connection outside the analyte. Few examples are present in literature of successful attempts and here significant ones are exposed.
In 2016 Lee at al.[11] demonstrated the use of EIS for cells encapsulated in an alginate hydrogel matrix. They reported GFP-expressing human breast cancer cells (GFP-MCF-7) cellular activities, such as cell proliferation and apoptosis, in a cell capacitor sensor made of vertical electrode, as shown in Fig.1.4(a) schematically. In Fig.1.4(b) and (c), the main results of their work are shown: in (b) the time dependence of capacitance, proving

proliferation of cells, and in (c) the capacitance dependency on cell density, as different curves highlight various cell concentration . Hence, capacitances increases according to the number of cells present in the hydrogel and it was also found that such results were not affected by alginate concentration. To monitor cell proliferation and migration a frequency of 1 kHz was set, without considering changing in the whole spectrum.

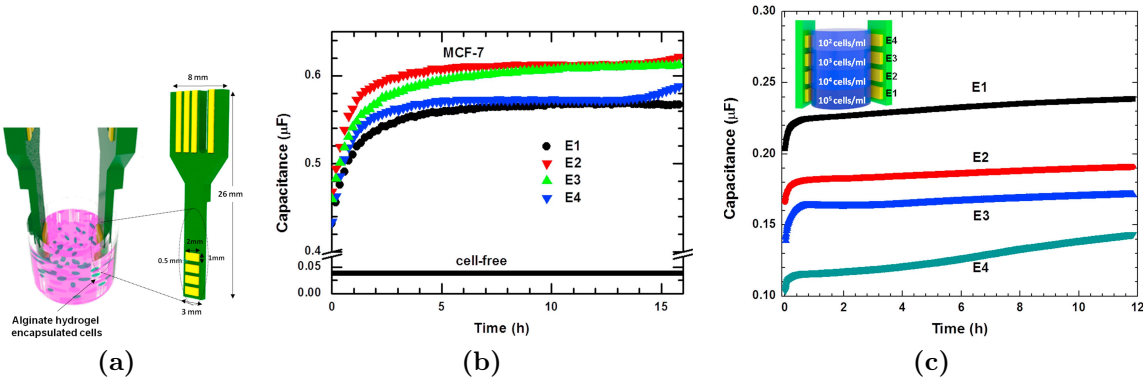

Figure 1.4: . Schematics (a) of a 3D capacitance sensor consisting of four pairs of vertically aligned electrodes.(b) Real time capacitance measured with electrodes in cell-free and GFP-MCF-7 cell-encapsulated hydrogels (E1-E4). (c) Comparison of real time capacitances having different cell density, proving the use of this sensor for cell counting. From [11].

Another configuration of electrodes was presented by Lei at all. [20] in a spheroidal culture of cancer cells. All electrodes were in-plane, as shown in Fig1.5(a), to monitor spheroids formed in an agarose hydrogel by the hanging drop technique. The optimal frequency was chosen again to be 1 kHz and in Fig.1.5 (b) the changes in impedance are visible, perfectly correlated to different cell densities. Larger variations in impedance magnitude are found at lower frequencies, but the authors consider them as an effect of increasing noise, as the noise is proportional to 1/f.
As inserting standard metal electrodes in a 3D culture can be very tricky, Del Agua et al.[21] implemented the idea of using conductive materials for scaffolds so that they can directly constitute the sensing electrode. Exploiting a porous scaffold based on poly(3,4-ethylenedioxythiophene) (PEDOT):xanthan gum, cells growth was promoted electrically and additionally checked by means of EIS. Those scaffolds were prepared by freeze-drying a PEDOT:xanthan divinyl sulfone (DVS) dispersion so the polymeric network is preserved and create cavities in which cells are seeded. Connecting it on a gold coated glass, the system can be monitored, as shown in Fig1.6(a). The impedance spectra acquired are pictured in Fig.1.6(b), with frequencies between 0.1 and 100 kHz; interestingly, they are not effected by the high noise at such small frequencies. Nevertheless, the main drawback of the experiment is the possibility of influencing cell behaviour and function while performing impedance tests, since the scaffold/electrode changes properties, as proven in various studies [22, 23]. In this sense, a cross validation of data must be

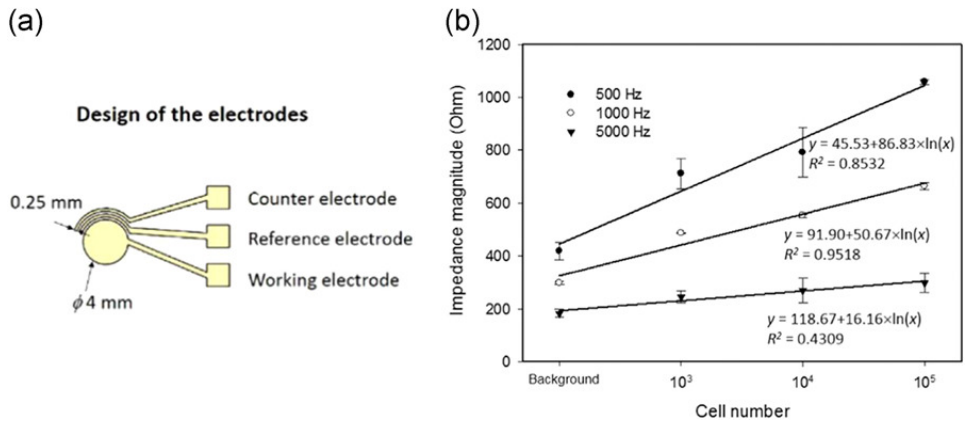

Figure 1.5: (a)Horizontal electrodes design for measuring impedance changes in spheroids enclosed in agarose alginate microwells. (b) The correlations between cell number in the hydrogel and the impedance magnitude measured at 500, 1000, and 5000 Hz. The error bars represent standard deviations of at least 3 repeated experiments. From [20]

undertaken in order to tell apart such influences. This implies that the scaffold traits, its potential use as a working electrode, and the characteristics of the 3D model (tissue or spheroids) all play a considerable impact in the measurements ultimate outcome, and as a result, models are required to compare the results with theoretical systems.

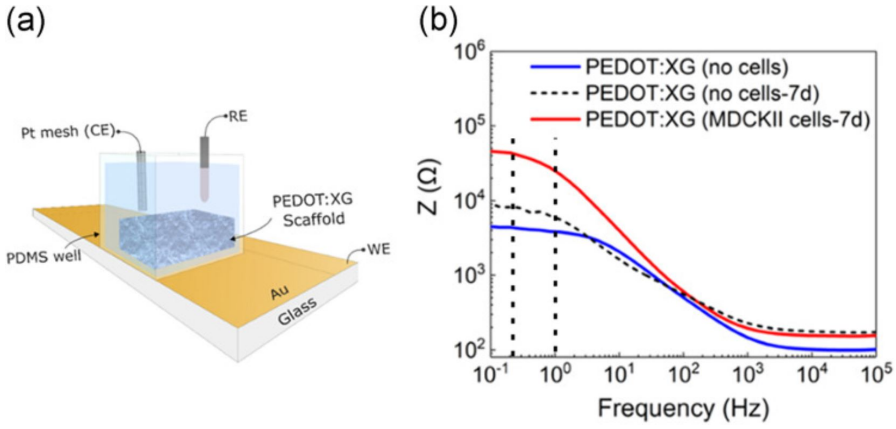

Figure 1.6: (a) Experimental set up for cell growth and monitor in a PEDOT:xanthan scaffold used as working electrode. (b) Impedance spectra obtained with this set up. [21].

In comparing 2D cell circuit with 3D cell culture, it was found an extra resistance associated to the matrigel matrix, in parallel with standard components representing cell impedance[14]. Indeed in 2D cell culture cells are in direct contact with electrodes while for 3D cell culture they are usually covered in an external matrigel matrix and seldom contact the electrode.
An example of coculture system monitored using the whole EIS spectrum is given by Groeber et al. [24]. They used parallel electrodes to analyze the integrity of reconstructed

human epidermis at different level of maturity. The equivalent circuit was made of n parallel resistor-capacitor, each corresponding at the different phases (Fig.1.7(a)). The data obtained at 1 kHz, in Fig.1.7(b), were validated with isolated human epidermis, proving that the artificial epidermis has the same electrical characteristics at 9-12 days of culture.

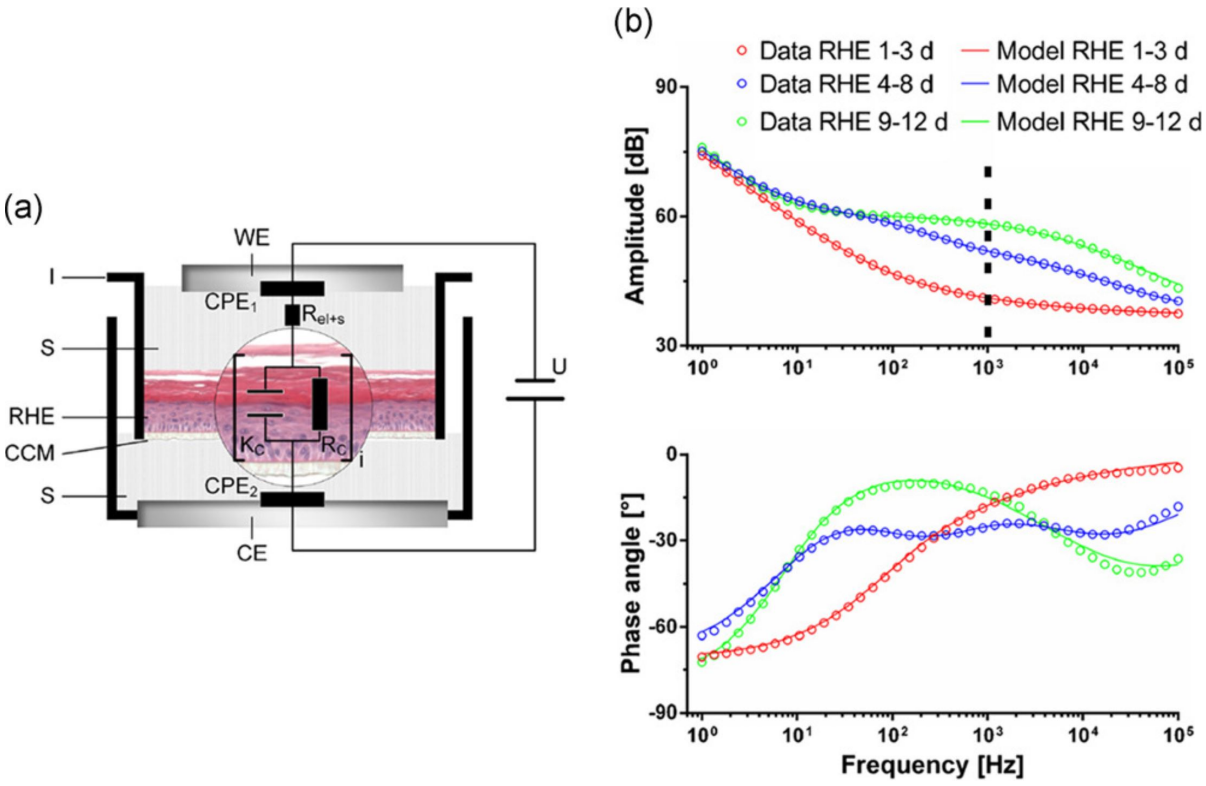

Figure 1.7: Parallel impedance electrodes to measure the maturity of a reconstructed human epidermis (RHE). (a) Detailed view of one measurement chamber with a RHE in a transwell insert and equivalent circuit. (b) Bode plots of impedance spectra from RHE at different time points.

1.2 Hydrogels for cell culture

The significance of the extracellular environment in controlling cell activity has been recognized more and more in recent years. Cell function can be considerably impacted by mechanical, structural, and compositional cues acting alone or in combination. Our knowledge on many cell-based processes is mainly derived from experiments on flat, stiff materials, like glass or polystyrene. Although these platforms' simplicity is appealing, cells cultivated on them frequently exhibit aberrant characteristics, including flattened shape, improper polarisation, altered responsiveness to medication, and loss of differentiated phenotype[25]. Furthermore, as already stated, these systems are typically 2-dimensional, whereas cells in the body are likely to receive signals in all dimensions. To bridge the gap between conventional culture systems and native complex systems, a variety of biomaterial systems have been created, including fibrillar foams, elastomeric films, patterned glass substrates, and hydroxyapatite ceramics. Yet, crosslinked hydrophilic polymers swollen in water, known as hydrogels, are appearing on the scene as a very promising choice for a wide range of cell culture applications, revealing fundamental phenomena regulating cell behavior and providing tools for the expansion and directed differentiation of various cell types, that are not possible with conventional culture substrates.
It would be impossible to cover all the advantages of using hydrogels here, since they strongly depend on the purpose of the study and on the type of cells under study: for example, for epithelial cells it would be important to consider adhesion and not toxicity towards polymerization radicals since they would be cultured after hydrogel formation, while other cell types are prior encapsulated in the liquid precursor and then the system is assembled through crosslinking. Therefore, only few general concepts are presented, alongside with a schematic synthesis of most common hydrogels in Table1.1 extracted form[26], focusing then on ionically crosslinked alginate hydrogel that is the one selected for this work.
Because of their high water content and soft texture, hydrogels cause the least amount of damage to the surrounding tissue and are compatible with living tissues and proteins [27], also facilitating transport of oxygen, nutrients and waste, as well as soluble factors[28]. They are especially appealing for the engineering of soft tissues since they have similar mechanical properties and morphologies, that can be plastered to mimic tissue morphology. It has been demonstrated that morphology alone can affect delicate cellular functions like proliferation, apoptosis[29], differentiation, and gene expression[30].
Additionally, many hydrogels can be created in moderate, cytocompatible conditions and are simple to modify to include desirable degradability, and cell adhesion ligands[31].
Particularly important are the so called *smart hydrogels*, materials with engineered chemical and physical properties so that are able to respond to external stimuli like temperature, pH, light, magnetic and electric fields, ionic strength, or enzymatic environment [32].
Numerous materials can be used in cell studies and broadly can be divided into natural or synthetic hydrogels. Natural gels for cell culture are typically composed of proteins

and elements of the extracellular matrix (ECM), such as collagen [33], fibrin[34], Matrigel, hyaluronic acid[35], or materials derived from biological sources, like chitosan[36], alginate[37] or silk fibrils. They are inherently biocompatible and bioactive, as they promote many cellular functions due to the myriad of endogenous factors present[38]. Contrarily, hydrogels can be created entirely from synthetic molecules, such as poly(ethylene glycol)[39], poly(vinyl alcohol)[40] and poly(2-hydroxy ethyl methacrylate)[41]. They serve primarily as a template for cell growth and lack the endogenous elements that encourage cell functions.

Material	Example vendors	Notable material features
Natural materials		
Collagen	BD BioSciences, Advanced BioMatrix (PureCol, FibriCol), Vitrogen, Flexcell (Thermacol, Collagel)	Typically sourced from rat tail tendon or bovine skin and tendon Usually purchased in pepsin- or acid-solubilized form and stored at low pH and temperature Enzymatically degradable Exhibits structural and mechanical properties reminiscent of native tissues Presents native cell adhesion ligands
Fibrin	Baxter (Tisseel, Artiss), Johnson & Johnson (Evicel), Sigma	Typically sourced from human plasma Enzymatically degradable Provides good substrate for studying wound-healing phenomena *in vitro* Low mechanics limit utility
Alginate	NovaMatrix-3D, PRONOVA (FMC BioPolymer)	Derived from brown algae Must be modified with adhesive ligands for cell attachment Ionic crosslinking with divalent cations enables easy cell encapsulation and recovery Additional covalent crosslinking often needed for strength
Synthetic materials		
Polyacrylamide (PA)	Sigma	Wide range tuning of substrate mechanics Probably the most standardized material as far as protocols for making hydrogels and using for culture Suitable for 2D cell culture only
Polyethylene glycol (PEG)	QGel Inc. (QGel), Sigma, Cellendes (3-D Life Dextran-PEG or PVA-PEG), BioTime Inc. (PEGgel)	'Blank slate' synthetic material enables a wealth of user modifications Premodified versions and various molecular weights are readily available Can be engineered to present different adhesive ligands and to degrade via passive, proteolytic, or user-directed modes
Hybrid materials		
Hyaluronic acid (HA)	Lifecore (Corgel BioHydrogel), BioTime Inc. (HyStem), BRTI Life Sciences (Cell-Mate3D)	Usually produced via bacterial fermentation, but can also be sourced from animal products Wide variety and high degree of potential chemical modification enables considerable tunability Interacts with cell receptors but must be modified with adhesive ligands to permit cell attachment
Polypeptides	Corning (PuraMatrix), PepGel LLC (PGmatrix), Sigma (HydroMatrix)	Typically formed by self-assembly Useful in soft-tissue applications and in conjunction with other materials Protein engineering enables great design flexibility

Table 1.1: Representative hydrogels that can be used for cell culture studies, including commercial vendors and the advantages and disadvantages of using each material [26].

1.2.1 Alginate

Alginates are groups of linear anionic polysaccharides derived from different type of harvested brown algae [42]. They are biocompatible and biodegradable in the body[43–45], rich in source and easy to obtain and, for those reasons, they have been widely employed in the food industry and have developed into very important biomaterials for pharmaceutical and biological purposes.
Chemically, alginates are copolymers which consist of linear (unbranched) 1,4 linked residues of β-D-mannuronic acid (M) and its C5-epimer α-L-guluronic acid (G), arranged in homopolymer blocks, i.e. GG or MM, or heteropolymer blocks (Fig.1.8), made of randomly coupled G and M units (GM or MG blocks). The linkages in the equatorial/axial or axial/equatorial position of the MG or GM blocks, the diaxial position of the GG blocks, and the diequatorial position of the MM blocks result in flat ribbon-like structures for the MM blocks, rigid folded structures for the GG blocks, and helix-like structures for the MG or GM blocks, respectively.

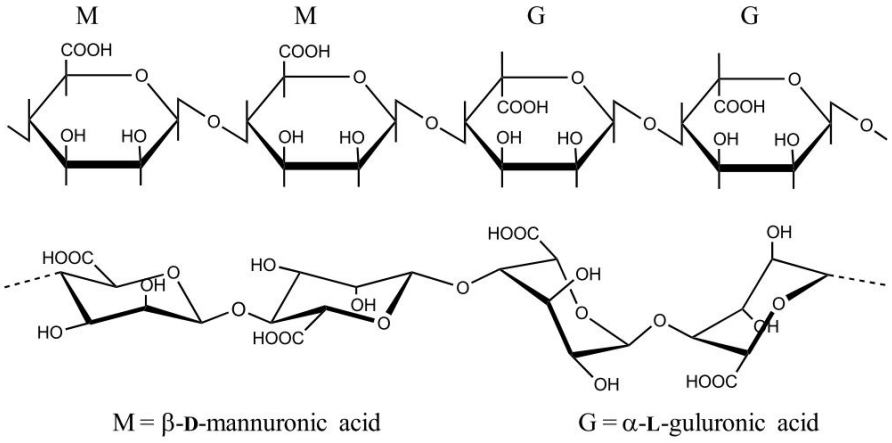

Figure 1.8: The structure of alginate shown as gropus of MMGG residues and respectively conformations. D-Mannuronic acid is ${}^4C_1$ with diequatorial links while L-guluronic acid is ${}^4C_1$ with diaxial links.

Molecule Rigidity/Flexibility, Solubility and Viscosity

Depending on the biological source of extraction, the growth, and the seasonal condition of the plant, alginate exhibits a wide range of chemical compositions and ratios of G and M residues[46]. The length of the G chain and the high G content are generally associated with high alginate chain rigidity, due to the greater hindrance of the rigid six-membered sugar rings and restricted rotation around the glycosidic bonds, as well as the electrostatic repulsion between the charged groups on the polymer chain[47]. Alginate high in G can create strong, brittle gels, whereas alginate high in M can create softer, more elastic gels. Alginate shrinkage and increased flexibility are caused by MG-blocks[48].

Unlike its monovalent salts and esters, which are water-soluble and create a stable, viscous solution, alginic acid is insoluble in water and organic solvents [49]. The solubility of alginate is affected by 4 parameters: (1) the distribution of G and M blocks, since highly-containing G blocks are more soluble than the ones with higher M concentration; (2) the pH value of solvent (for low pH only alginate with high content of MG-blocks are soluble); (3) the ionic strength; (4) the presence of gelling ions.
When alginate is dissolved in water, the volume can swell 10 times and the viscosity of the solution is then influenced by molecular weight, rigidity, extension of the chain of the polymer and ionic strength of the solution. The viscosity rises with increasing molecular weight, alginate concentration, or stiffness of the constituent chain blocks, as well as with the extent of the chain, due to electrostatic repulsion among charged groups [46].

Gelation properties

The possibility of alginate to produce ionic gels in the presence of polyvalent cations is their most crucial characteristic. The process of gelling involves an ion exchange between the monovalent sodium ion (Na^{+}) present in alginate solution and other, albeit polyvalent cations (most frequently calcium, Ca^{2+}), followed by the coordination of the latter with the alginate macromolecule.
An intermolecular gel network is created as a result of the cooperative binding of two successive residues in various alginate chains (Fig1.9(B)), which occurs in the chelation of the gel-forming ion between two consecutive residues (Fig.1.9(A)).

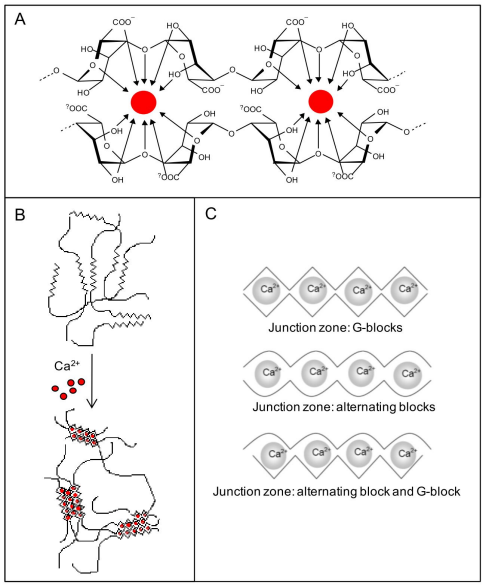

Figure 1.9: Four consecutive G-residues from two chain segments of one or two alginate molecules creating a binding site for divalent cations (A). Formation of an intermolecular network of alginate molecules formed in presence of gelling ions such as Ca^{2+} (B). Gelling ions organized in alternative junction zones (C) [50].

Alginate hydrogel primary structural components are G-blocks, but also alternating blocks can play a role in gel formation [51]. This structure is know as egg-box model of alginate gels. Fig.1.9(C) illustrates the many junction zones in an alginate gel. Nevertheless, a 3/1 helical conformation of G blocks was found to be more appropriate for Ca alginate gels formed slowly, while the 2/1 helical conformation is still possible in fast gelatinized Ca-alginate, in which the 2/1 helix is a metastable form [52].
In contrast to most gelling polysaccharides, alginate gels have the particular feature of being cold setting. In principle, this implies that alginate gels set more or less independent of temperature. The kinetics of the gelling process may, however, be strongly modified by a change in temperature. The properties of the final gel will also change if gelling occurs at different temperatures, due to the non-equilibrium property of the alginate gels[53]. Another implication of thermo-irreversibility is that alginate gels are heat stable.
Since the gelling of alginate cannot be controlled by temperature, other parameters impacting gels quality must be considered, such us type and concentration of crosslinking agents/cations, molecular weight, composition, degree of polymerization and polymer chain length of the alginates.
Alginates have different affinity for divalent cations in an increasing manner as Ca^{2+}<Sr^{2+}<Ba^{2+}. The cation size may influence the Young's modulus of gels: larger cation have stronger binding forces at junction zones thereby creating stronger gels [54]. Trivalent cations such as Al^{3+} and Fe^{3+} can also be used to gel alginates and, due to the ability to bind with three carboxyl groups from several alginate polymer chains simultaneously, they produce a more compact gel network.
Increasing the content of G residues in the chains or, similarly, molecular weight result in more strong and brittle gels[55], as alternating MM and MG blocks have a lesser affinity for the cation.

1.2.2 Ionically crosslinked alginate hydrogels as scaffolds for 3D cell culture

Alginate is notable for its ability to create hydrogels through ionic crosslinking[1], as said previously, which recently have been investigated as scaffolding materials for 3D cell culture studies and tissue engineering. There are several approaches and adaptations of 3D cell culture and alginate offers a fantastic toolbox for design and optimization, as can be seen in this section, even though one system is unlikely to fit all types of research or cell types. Two properties have to be considered: mechanical properties in order to better match the native system and the degradation behaviour; additionally, there are situations when it may be preferable to encourage particular cell-alginate gel interactions.

[1]It is, actually, possible to obtain even covalent crosslinking from chemically modified alginates, which provides adjustable physical properties[56], but it represents a less common and more complex method, since often the crosslinking agents are toxic and need to be removed.

Mechanical properties and degradation

Physical elements like the cross-linking density, cross-linker type, and molecular weight distribution can impact on mechanical qualities like stiffness and swelling (independently), in addition to chemical modification of the polymer [57].
Conventionally, hydrogels are formed through interaction of solutions of gelling ions and polymer. Increasing polymer concentration in the solution leads to higher stiffness, especially for high molecular weight[58]. This in turn leads to an increased viscosity of the pre-gelled solution; in order to overcome difficulties in processing of solutions, a combination of low and high molecular weight can be used. It was further demonstrated that the molecular weight predominates the mechanical properties at a low crosslinking density while the G content and average G-block length predominate the mechanical properties at a high crosslinking density [59].
On the other hand, gelling conditions and type of cross-linker affect mechanical properties too. Low temperatures slow down the rate at which Ca^{2+} ions diffuse, which results in slower cross-linking, a more ordered network structure and a longer gelation time[60], while normally gelation takes places instantaneously yielding not uniform structures with varying crosslinking density and a polymer concentration gradient. The composition of the aqueous phases is another affecting parameter, for example phosphate can binds Ca^{2+} temporarily and slow its diffusion, while higher calcium content can produce superior strength, i.e. higher Young's modulus[61]. In Fig1.10, these effects are presented evaluating compressive strength [59], varying gelling molecules together with calcium content in (a) and polymer concentration in (b).

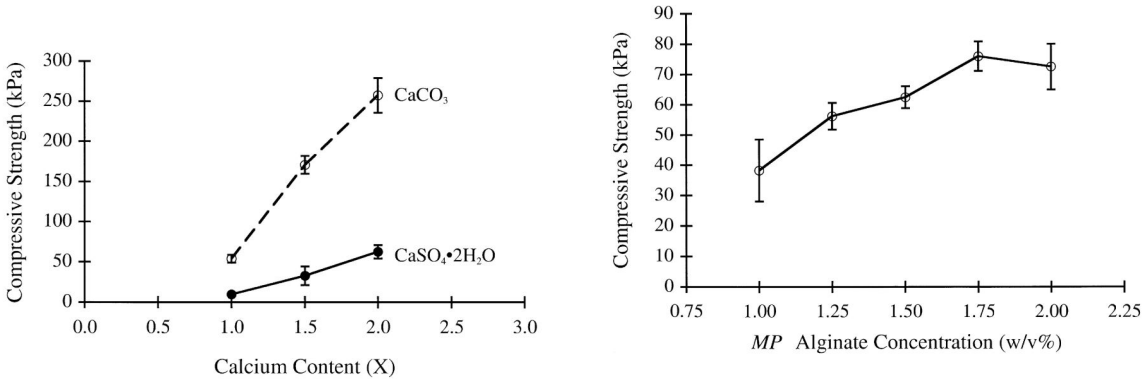

Figure 1.10: In (a): comparison of mechanical properties of alginate gels made with 100% $CaCO_3$-GDL versus those made with 100% $CaSO_4 \cdot 2H_2O$ as functions of calcium content. In (b): the mechanical properties of alginate gels versus alginate concentration. The alginate is called MP as it's derived form *Macrocystis pyrifera*. Graphs extracted from [59].

At neutral pH, ionically crosslinked alginate degrades spontaneously upon losing crosslinking ions [62]. Degradation can be controlled by adjusting the composition and molecular weight of the polymer, using two main methods: (1) high-molecular weight alginate can be gamma-irradiated to produce polymers with mismatches between crosslinking blocks leading to a more rapid displacement of cross-linking ions [63]; (2) partial oxidation, as alginate can be made susceptible to hydrolysis via reaction with sodium periodate[64].

Cell interaction

Alginate itself does not support cell attachment. However, cell adhesion can be promoted by chemical manipulations coupling cellular adhesion molecules, such us laminin, fibronectin and collagen, to alginate scaffolds or by changing chemically the presentation of ligands which can interact with cells[64]. Different cell types may react differently to these cues though, while coupling whole molecules can result in non-specific interactions as it represents a hardly-controllable process [65].

Alginate hydrogels technologies

Four technologies of alginate hydrogels are shortly presented in this section and include beads, delayed gelation systems, macroporous scaffolds and 3D printed scaffolds. [2]

- *Beads*
  Alginate gel beads are frequently created by dripping a sodium or potassium alginate solution into an aqueous calcium ion solution, which is normally made of calcium dichloride ($CaCl_2$). Cells are dispersed inside the alginate solution and so are encapsulated inside the droplets. Because of the alginate beads porosity, cell byproducts like proteins can diffuse out of the gel while oxygen and nutrients can diffuse into the gel. Macrophages and other immune cells, or antibodies, can also pass through the hydrogel porous barrier.
  It has been established that encapsulation in an alginate hydrogel is a quick, safe, and adaptable approach for immobilizing macromolecules and cells; this method can be used for treating/study several diseases, including Parkinson's disease, liver failure, hypocalcemia. Generally, in those applications the droplet size is the most important parameter and it is usually regulated to give beads of 100-200 μm diameter [50].

[2] Other technologies providing 3D cell culture in alginate scaffolds are honeycomb alginate scaffolds with an aligned pore structure for improved vascularization [66], scaffolds impregnated with magnetically responsive nanoparticles for stimulation of cells and induced organization of endothelial cells into capillary-like structures [67], and alginate scaffolds with controlled nucleation of hydroxyapatite generating a composite scaffold promising for bone tissue engineering [68].

- *Delayed Gelation Systems*
  In this case gels are formed *in situ* on patients, enabling implantetion with less invasive surgery and precise deliver. To have delayed gelation a mixture of alginate and gelation ions is formed and the internal gelation properties of the system are considered. Examples include mixing of an alginate solution with a suspension of calcium alginate particles [69], calcium carbonate and GDL [70] or calcium sulfate [71].

- *Macroporous Scaffolds*
  Macroporuous scaffolds are large construct in which cells are seeded inside the hydrogel network itself. Their benefits include enhanched mass transfer of nutrients, oxygen and removal of waste, along with predefined dimensions and pore size and better resistance to deformation. On the contrary, since the pores are frequently either too small to let cells in or too large to retain cells inside, a significant problem with such scaffolds may be cell seeding efficiency and cell distribution.
  Nevertheless, two alginate based macroporous systems for cell culture are already commercially available, AlgiMatrix and NovaMatrix-3D from Thermo Fisher Scientific/Life Technologies (Carlsbad, CA, USA) and FMC BioPolymer/NovaMatrix (Sandvika, Norway), respectively.

- *Alginate as a Bioink and 3D Bioprinting*
  Nowadays, 3D printing is extremely used in industry and home-use application. The possibility to create bespoke three-dimensional structures on demand using only basic components is already been applied in tissue engineering and regenerative medicine[72].
  Extrusion and ink-jet 3D bioprinting processes both require biocompatible "inks." Due to its compatibility with cells, simplicity in creating cross-linked hydrogels, and capacity to regulate biodegradation, alginate has demonstrated particular relevance as a bioink. Numerous examples are reported in literature [73–77] and all show a high cell viability after bioprinting($>80\%$) [50].

1.3 Bio compatible conductive materials: conjugated polymers

In the processes of developing new technologies, materials are often the main limitation. Materials currently used for devices in our daily lives are based on electron or hole charge transport, in strong contrast with the biological world. Taking into account our case of interest, it is widely known that cells communicate through unique structures such as ion channels, ion pumps, gap junctions and receptor/transporters molecules based on ion currents, making difficult to transduce signals across biotic/abiotic interfaces. Bio-compatibility and flexibility in matching stiffness, size and curvature of human tissues have brought to the rise of conducting polymers in bio electronics (Fig1.11). The majority of work has been on conjugated polymers (CPs), thus the discussion will be focused on them and on the one with the biggest prospects in bioelectronics, poly(3,4-ethylenedioxythiophene) doped with poly(styrenesulfonate) (PEDOT:PSS).

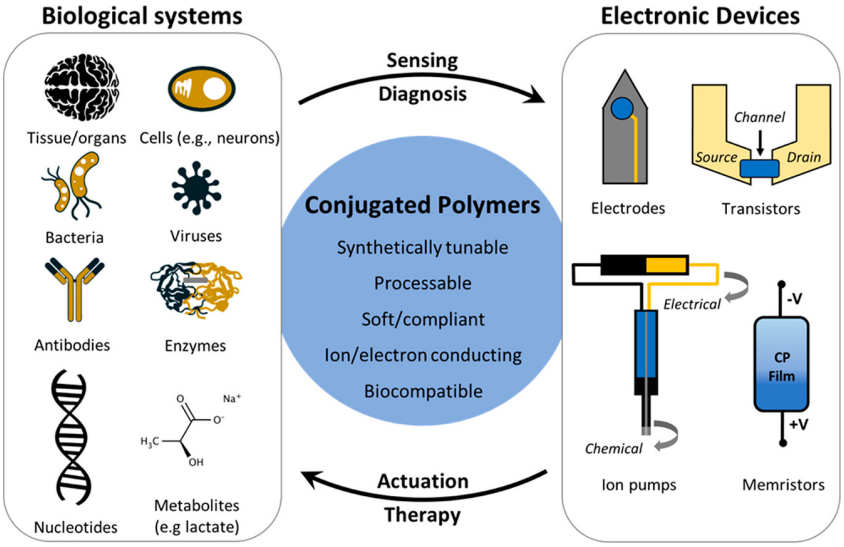

Figure 1.11: The unique set of properties of conjugated polymers that lead to state-of-the-art devices used for sensing or actuation[78].

1.3.1 What makes CPs promising for bio interfacing?

Planar, stiff aromatic repeated units constitute CPs, which often serve as templates for extended ribbon-like macromolecular conformations. A combination of relatively weak van der Waals intermolecular associations from side chains and aromatic π stacking, as well as both dipolar interactions and electrostatic forces, results in a thin-film microstructure that promotes electronic coupling between chains, which is necessary for charge transport (when doping is present). Indeed, the alternating single and double bond structure in the

conjugated backbone make carbon atoms able to conduct electrically: thanks to the sp^2 hybridisation of carbon, the p orbitals in one direction, conventionally in the Z-axis, can align parallel to each other, forming a continuous π bond along the chain shared among atoms. Delocalized π-electrons can move freely in the unsaturated backbone forming a pathway for mobile charge carriers. However, the energetic band structure does not correspond to a continuous half occupied band, but, given the distortion along the chain introduced by different bond lengths, to a completely full band π and a completely empty band π^*, separated by an energy gap given by the energy difference between the highest occupied molecular orbital (HOMO) in the band π and the lowest unoccupied molecular orbital (LUMO) in that π^*.
Most CPs do not have intrinsic charge carriers and, therefore, external particles are needed, similarly as in semiconductors doping: polymers are partially oxidised by electron acceptors and partially reduced by electron donors. Once doped, they can be either p-type, transporting holes, n-type, for electrons transport, or be ambipolar (supporting both hole and electrons transport) and, importantly, they can also act as ion transporters. CPs show mixed electronic and ionic conducting mechanisms, emerging as optimal candidates for investigating biological events, as often they involve ion fluxes in aqueous environments. Electrical and physicochemical features are greatly and reversibly modified by loading ions inside the structure, in a process known as electrochemical doping/ dedoping[78]. The mobility of ions in the film is promoted in transport areas that can be hydrated; particularly, close to the backbone ion penetration is favoured by Coulombic attraction from the increased polaron density of the conjugated systems. Any variation of the charge density (for example, by ion uptake) greatly impacts the morphology and electronic characteristics, i.e., the film microstructure, due to the considerable distortion of the local molecular environment that might result from polaron production in the CP; contrary to inorganics where such changes cannot effect rigid lattices.
The nature and arrangements of bounds renders CPs "soft" materials, which contributes to their ability to swell. Thus, as large volumes of medium can be absorbed, more ions or biomolecules are available and ion transduction is enhanced. The mechanical compatibility with vary substrates, like glass, plastics or paper, is another strength related to CP softness, enabling manufacturing of flexible, stretchable electronics. This characteristic makes low-temperature solution processes possible, allowing to treat materials with standard procedures such as spin coating, printing, and vapour-phase deposition, as well as experimenting with enzymes and other biological entities which degrade under extreme conditions.
Moreover, thin films CPs are typically transparent, which grant analysis with optical techniques.
Desired chemical and physical properties can be tuned easily in CPs. For example, adding chemical moieties on the polymer backbone can improve their electronic performance, or binding molecules of interest for specific stimuli responsive platforms or adhesion on specif target surfaces can result in composite materials. Even polarity of charge transport

can be controlled by chemically manipulating the energy gap. The size, shape, and composition of the side chains can all affect aqueous and ionic absorption, which in turn affects thin-film morphology and, consequently, transport properties.

1.3.2 PEDOT:PSS - an emerging material in bioelectronics

After Professors Heeger, MacDiarmid, and Shirakawa discovered electrically conducting polymers (Nobel Prize in Chemistry 2000), and more than 30 years of worldwide intense research and significant efforts, PEDOT, or poly(3,4-ethylenedioxythiophene), sets numerous benchmarks for the entire field. PEDOT, developed by Bayer AG, Leverkusen in 1988, is perhaps the best conducting polymer available in terms of conductivity, processability, and stability[79].
PEDOT has an high and stable conductivity (around $10^3 S \cdot cm^{-1}$, varying according to dopant and polymerization), expecially in its doped state, and can be synthesised by standard oxidative chemical or electrochemical polymerization methods of 3,4-ethylenedioxythiophene (EDOT), shown in Fig.1.12.

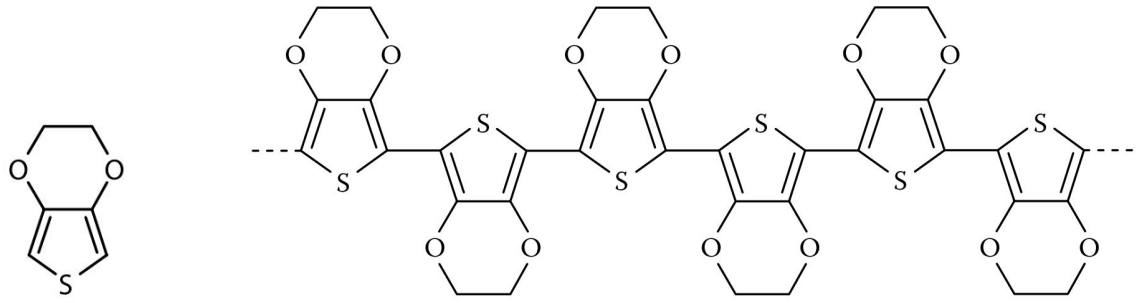

(a) *EDOT* **(b)** *PEDOT*

Figure 1.12: Chemical structure of (a) 3,4-ethylenedioxythiophene (EDOT) and (b) PEDOT, or poly(3,4-ethylenedioxythiophene)[79].

There are several reasons that justify the great success of PEDOT in industrial applications. First of all, it can be reversibly and repeatedly doped and undoped and this is followed by a change in colour, from opaque blue in the reduced state to almost transparent in the oxidized state[80]. It has an excellent chemical and thermal stability (below 150°C), thanks to favourable ring geometry and the presence of low defects given by a very regular chemical structure[81]. In addition, PEDOT has a low redox potential: according to cyclic voltammetry, cycling has no effect on the redox peaks at about 0 mV (oxidation) and -400 mV (reduction)[82]. Measurements of the open circuit potential reveal that the neutral films are rapidly oxidized, whilst is stable only for negative potential applied of -700 mV[83].

Above all of the former reasons, one of PEDOT main advantages and propably the main reason of its widespread use is its availability as a polymer dispersion: a polyelectrolyte complex (PEC) can be created using poly(styrenesulfonic acid) (PSS) as a counterion to create a stable dispersion, so that the positive charges on PEDOT are balanced, by the fixed PSS anion, in the chemical structure presented in Fig.1.13. PSS is always

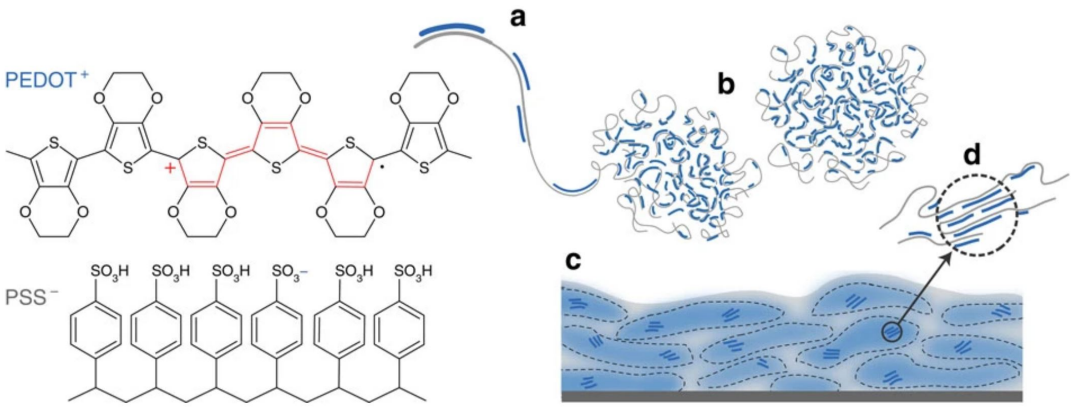

Figure 1.13: The chemical structure of PEDOT:PSS and commonly described microstructure of the system: (a) synthesis of PEDOT onto PSS template, (b) formation of colloidal gel particles in dispersion and (c) resulting film with PEDOT:PSS-rich (blue) and PSS-rich (grey) phases. (d) Aggregates/crystallites support enhanced electronic transport.

used in excess as host polyelectrolyte (HPE), with PEDOT to PSS standard weight ratio ranging from 1:2.5 up to 1:20. Similar to most charged conjugated polymers, the PEDOT polycation is not soluble in any solvent. Therefore the synthesis of this polycation needs to be performed in the presence of PSS so that the PEC complex is formed in situ as the polycation chain grows. Water is the solvent of choice for the PEDOT:PSS synthesis because it is highly polar, a suitable PSS solvent, and inert to the majority of oxidising and reducing chemicals. There is no molecular or supramolecular order in the resulting PEDOT:PSS, only a random interaction between polymer chains, due to the delocalization of positive charges in PEDOT, the weak polar groups, and the different spacing of PEDOT charges compared to those in PSS [79].
The dispersion can be described as a loosely crosslinked and highly swollen polymer gel network, composed of gel-like PEDOT-enriched particles and polyanion PSS-rich shells in a aqueous solvent[84]. The gel particles (Fig.1.13(b)) exhibit π-stacking and deposit in what has been called a pancake-like morphology[85], shown in Fig1.13, where gel particles shrink in the vertical direction during the film formation, having in the end a disc-like shape with PSS-rich region in the contact area.

1.3.3 PEDOT:PSS thin film properties

As most of electronics are developed in planar settings, illustrating film properties of PEDOT:PSS is crucial to understand how this PEC entered so widely in the industry field. Hence, the main properties are listed below.
Foremost, deposition of PEDOT:PSS dispersion in water is possible with all common technique available for uniform coating. Few examples are slit coating, drop casting, bar coating, spin coating, electrospinning, and spraying, but also screen printing, inkjet and nozzle printing for more specific structures. To ensure uniformity of films, viscosity, adhesion to substrates and surface tension need to be considered and accordingly adjusted. Many protocols exist and all are based on using different ratios of PEDOT to PSS or adding of additives.

Thermal stability and durability

For processing of PEDOT:PSS films, water needs to be removed usually trough baking or applying IR radiation or in combination of both.

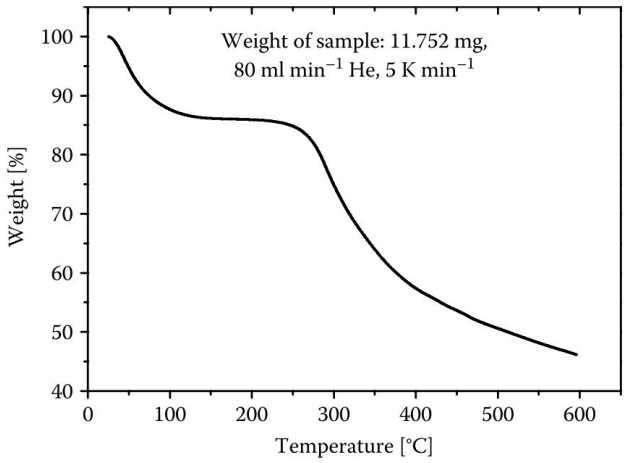

Figure 1.14: Thermogravimetric analysis (TGA) of PEDOT:PSS with a ratio of PEDOT to PSS as 1:20 by weight, conducted by Bayer Technology Services, Leverkusen, 2006.

In this sense, the exceptional thermal stability comes in great help: the thermogravimetrical analysis, shown in Fig.1.14, of thick layers conducted by Bayer Technology Services proves that between 100°and 200°C the weight loss is only due to evaporation of water without degradation of samples. Around 250°C is observed a high drop in weight, corresponding to the onset of the first polymer degradation associated to the loss of sulfonate groups in PSS chains. It undergoes a second degradation for temperature above 350°C, that involves oxidation of carbon atoms.
Although PEDOT has a steady conductivity, it can degrade when subjected to severe conditions (like happens for all carbon-based compounds). As a result, PEDOT:PSS light stability has been thoroughly studied[86], and the decay process was discovered to be connected to oxygen oxidation that is improved by light. In particular, it's proven that

films exposed to air and UV light (λ<320nm) show a steep increases in resistivity, while films protected from environmental conditions show a much slower and steady increase[79]. This finding demonstrated that degradation is caused by air-induced PEDOT oxidation, which is enhanced by concurrent light absorption. In general, protection form UV-light and temperature above 70°C should be taken, including the hermetic encapsulation of the device or blending of stabilisers, to ensure high and stable performance on conductivity. Another environmental condition to be taken into account is humidity. Like other polymers containing sulfonic acid groups, PEDOT:PSS is strongly hygroscopic. Comparing data presented in Fig1.15(a), most of water intake happens almost instantaneously or in few minutes after exposing to humidity. The kinetics of absorption depends, of course, on sample geometry and humidity level. In Fig.1.15(b), an increase of a 100 nm-thick film is proved to be correlated with high PSS content and humidity levels.

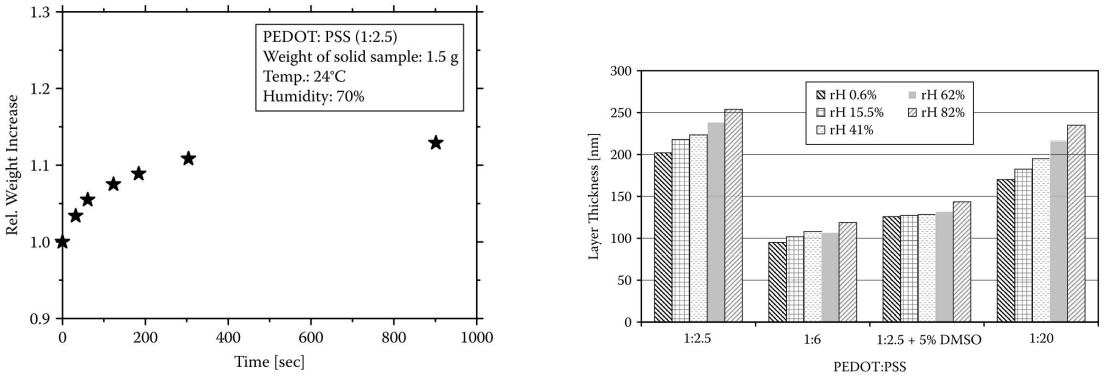

(a) **(b)**

Figure 1.15: In (a):PEDOT:PSS (weight ratio of PEDOT:PSS = 1:2.5) has been dried in a beaker in an oven to form a layer several micrometers thick and subsequently transferred into air with a relative humidity of 70%. The weight increase owing to the absorption of water is monitored as a function of time. In (b): Layer thickness increase of PEDOT:PSS film of 100 nm as a function of relative humidity for different ratios of PEDOT to PSS. Data from Bayer Technology Services, Leverkusen, Germany, extracted from [79].

Mechanical properties and morphology

The mechanical characteristics of thin films made of PEDOT:PSS were examined by tensile testing at various relative humidity levels by Lang et al.[87].
The fracture behaviour can be demonstrated to be substantially dependent on humidity and range from brittle to plastic. The polymer exhibits brittle fracture behaviour at rH = 23% which changes to plastic fracture behaviour at an intermediate rH = 55% (Figure1.16). The Young's modulus of films increases from 0.9 GPa at 55% rH to 2.8 GPa at 23% rH. When samples were examined at 55% rH, the surfaces went from being smooth at 23% rH to being rough with shear lips.

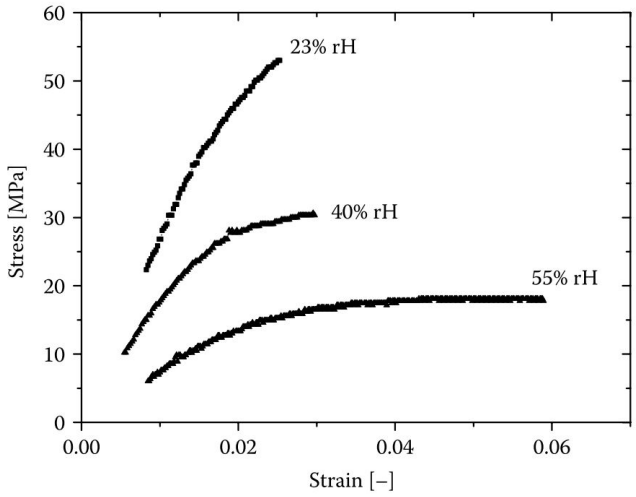

Figure 1.16: Stress–strain diagrams of PEDOT:PSS at different levels of relative humidity, from [87].

PEDOT:PSS films are amorphous: using x-ray diffraction (XRD), no crystalline regimes other than short-range order have been discovered[88]. Based on the insights gained during tensile tests, scanning electron microscopy (SEM) and atomic force microscopy (AFM) analysis and in agreement with the results in literature[89, 90], a model was presented[87]: grain of diameters approximately of 30-40 nm, with PSS-rich shell and PEDOT-rich core, compose the whole film. Hydrogen bonding between PSS within the shell gives this structure coherence, but, since these bonds are highly strong at low relative humidities, they cause transgranular fractures that lead to brittle macroscopic fracture. Higher relative humidities then cause the hydrophilic and hygroscopic PSS-rich shell to absorb more water, resulting in a swelling of the substance and wider spaces between grains. Greater separations between shells result in weaker hydrogen bonds, which reduces cohesion and, as a result, mechanical strength. At increasing relative humidities, individual grains can move past one another upon tensile pressure. This leads to a rough surface and an intergranular fracture, while plastic failure happens on a macro scale.

Electrical properties

Thiophene rings, composing PEDOT, create a π-system able to release free electrons, hence heavly p-doped. Indeed, this system generated one free charge every three to four thiophene rings, making PEDOT:PSS an intrisically conductive polymer with metal-like characteristic. Although PSS does not directly contribute to charge transfer, it acts as a template to keep PEDOT in the dispersed state, offers film-forming capabilities, and balances the cationic PEDOT charges to create a stable salt [79].

To comprehend electrical properties of a material, conductivity is a useful tool for characterisation. Even though a complete theory for conducting mechanism is not available for highly doped polymers, such as PEDOT:PSS, it is possible to start by the simple definition of conductivity as the product of elementary charge, charge carrier mobility and charge carrier density, considering both holes and electrons as charge carriers. In PEDOT:PSS only holes contribute to charge transport, while injected electrons recombined at the oxidizìsed PEDOT sites. Hole density can be calculated by geometry considerations and depends on PEDOT to PSS weight ratio. For a ratio 1:2.5 the hole density is estimated to be $\sim 3 \cdot 10^3 cm^{-3}$ and therefore the conductivity is 1000 S/cm. Other factors can influence, tough, conductivity: as already mentioned, the distribution of gel particles change morphology and then conductivity and it can be obtained by adding other components; moreover, pH between 0-3 can boost conductivity[88].
Vary studies were conducted on the dependence on temperature[88, 91, 92], and all results were fitted into the *variable range hopping* model. In fact, charge hopping between nearby sites is a common explanation for the conduction mechanism of CPs [93]. Conjugated polymer segments are creating electrical active sites more frequently than other types because of their ease of oxidation or reduction. Conductivity increases with temperature (in a range of 0-300 K), with a trend given by:

$$\sigma(T) = \sigma(0) \cdot \exp(\frac{-T_0}{T})^{\alpha} \tag{1.3}$$

where $\sigma(0)$ is the conductivity at infinite temperature, $k_b T_0$ is the energy barrier between localised states and α is equal to $1/(1+\mathrm{D})$, with D representing the dimension of the system and assuming that the density of states near to Fermi level is constant or varies smoothly with energy. Moreover, the transport mechanism is one-dimensional for a high conductivity and three-dimensional for a low conductivity.

Chapter 2

Materials and methods

This Chapter presents and explains the specifics of the materials used together with the experimental methods for device fabrication and characterisation.
It's organised into 5 section, each treats of techniques used for each passage of this work, from fabrication to testing of the final device. The 2.1 and 2.2 sections are about the specifics on fabrication of the multi electrode arrays through lithography adapted to this case and the methods for production of calcium alginate scaffolds, while the results and its optimisation will be presented in the next chapter. The section 2.3 shows optical methods to validate results, while the 2.4 present briefly cell cultures methods and lastly in section 2.5 the set up used to verify electrically the functionality of the device produced is explained.

2.1 Fabrication of the multi-electrode array

The device is composed of a planar multi-electrode (from now on MEA), to which a film of calcium alginate hydrogels (CA) is attached patterned with pyramidal wells, named h-MEA, which will treated later on and in Chapter 3. The fabrication of the MEA is separated to the fabrication of CA scaffolds. It follows a standard lithography procedure, divided in different steps, plus an additional step with the functionalization of the surface to allow a CA scaffold to attach.

- **Step 0: glass substrate cleaning**
  The substrates were cleaned in four steps: first, glass slides were submerged for 10 minutes in an ultrasonic bath of soapy water (1/10 volume volume ratio), followed by a washing with distilled water. Substrates were dipped in acetone, isopropanol and distilled water, and the same procedure was repeated for each bath. Finally, a nitrogen flow was used to blow-dry the slides. The slides were next dehydrated by placing them on a hot plate at 110°C for 5 minutes in order to eliminate the adsorbed water on their surface. The photoresist adhesion is also enhanced by this passage. The substrates were ready for the following phase after cooling for 30 seconds.

- **Step 1: spin coating of positive photoresist**
  MicroChem S1818 positive photoresist (purchased by *micro resist technology GmbH*) was spin-coated on the glass substrates, using 1.8 mL of S1818 for each 50x50 mm slide. Spin-coating was performed at 4000 rpm. This angular velocity was reached in $t_{ramp} = 1$ s (4000 rpm/s acceleration), and maintained for $t_{dwell} = 60$ s. After spin-coating, substrates were annealed on a hot plate at 110°C for 1 min.

- **Step 2: photolithography of all components coated in gold**
  Using Durham Magneto Optics' ML3 MicroWriter, microlithography of sensing electrodes, pads, wires, and alignment components was carried out. ML3 is a direct-write photolithography machine. Traditional methods of photolithography typically include exposing through a chromium-glass mask made by specialised suppliers. It is frequently important to update the mask design in research situations. By holding the mask in software, direct-write lithography equipment (also called digital mask aligners or maskless aligners) get around this issue. Direct-write lithography uses computer-controlled optics to display the exposure pattern directly onto the photoresist rather than through a physical mask. CleWin 4 software was used to create the patterns, which were then imported into the microwriter control program. ML3 microwriter uses a 385 nm light source able to go down to 1 µm resolution. The light exposition on the photoresist was set to 250 mJ/cm^2.

- **Step 3: photoresist development**
  After microlithography, samples were immersed and moved gently in a beaker containing Microposit MF-319 developer for 45 s. Then, the same procedure was repeated in distilled water. As S1818 is a positive photoresist, the regions of the photoresist layer which had been exposed to the microwriter light became soluble to the developer and were removed during this procedure. Finally, samples were blow-dried with N_2 flow.

- **Step 4: metal evaporation**
  Gold pure at 99% and chromium were used for evaporation, in quantity of (20± 4)

mg for chromium and (170 ± 4) mg for gold. The metallic filaments were washed in an ultrasonic bath with acetone, isopropanol and distilled water, and sonicated for 10 minutes in each step. Then, they were placed on two different tungsten filaments inside an evaporation chamber. The two metals were deposited one after the other thanks to the evaporator's dual heat source. Chromium is deposited before gold since it serves as a precursor and has superior adhesion to slides. By activating a rotary pump and a molecular pump, the pressure inside the chamber was lowered to about 10^{-6} torr. The evaporator's power was then gradually raised in order to heat the crucible by intensifying the current running through the tungsten filaments. In particular, to prevent filament breaking, the power output has been increased by 5% every 30–40 seconds. Since impurities evaporate at lower temperatures than those of chromium and gold, the slides were covered by a suitable shield (known as a shutter) until the apparatus reached high temperatures. At that point, the shutter was then taken off, and the metals began to deposit one at a time until they completely evaporated. The power output of the evaporator was then steadily decreased until it was turned off. On each sample, a layer of chromium measuring 10 nm thick and a layer of gold measuring 60 nm thick were deposited on average.

- **Step 5: photoresist lift-off**
  Samples were placed in a container filled with acetone for 4 hours. Then, the container was sonicated for 10 s. During lift-off, acetone dissolved the photoresist and, consequently, it removed all the metallic layer which had been evaporated onto it. Samples were then immersed in a new container with fresh acetone and sonicated for 10 s to remove all remaining resist. This procedure was repeated in isopropanol and distilled water. Finally, samples were blow-dried with nitrogen flow.

- **Step 6: patterning of negative photoresist**
  Similarly for positive resist, the negative photoresist deposition needs three passages: spin-coating, exposition to light and development. To activate the surface, a plasma treatment is in advance performed (parameters: 55W, 255 Duty ratio, 1 min, Gas Air, 10 sccm). 3 mL MicroChem mr-DWL 5 was spin coated at 3000 rpm, witht_{ramp} = 1 s (3000 rpm/s acceleration) and t_{dwell} = 30 s. After spin-coating, substrates were annealed on a hot plate at 110°C for 2 min, letting resting at room temperature for 10 min. Using again MWL3, the light exposition was set at 300 mJ/cm^2. A post-exposure bake on a hot plate at 100°C for 2 min followed. It is required 1 h of cooling at room temperature. Then the development was obtained by moving the samples gently in mr-Dev 600 developer for 1 min and 30sec, then rinsing them for 1 min in isopropanol and drying under N_2 flow. Lastly, a second annealing was performed: starting at 80°C, the temperature was raised at intervals of 10 min and 40°C, until reaching 140°C at which was left for 40 min. Those annealing treatments

serves as they harden the resist and make it more resist to external stress.

- **Step 7:patterning of the PEDOT:PSS thin film**
  Step 1 was repeated using MicroChem maP-1275 G, that creates a thicker layer. Then, photolithography and development were performed by repeating steps 2 and 3, changing light exposition at 1150 mJ/cm^2. After these passages, we expect the irradiated region of the surface to have a trapezoidal structure, because the internal part of photoresist was more sensitive to the light exposure and was more erased with respect to the external one. This structure can be exploited to reduce the broadening of the PEDOT:PSS pattern. In fact, once the film is deposited, PEDOT:PSS chains tend to crosslink between the developed and not developed regions of the sample surface, increasing the film broadening after the photoresist lift-off. The trapezoidal structure should prevent the (vertical) crosslinking, giving to the film a less broadened boundary.

- **Step 8: preparation and deposition of the PEDOT:PSS solution**
  The active region of the devices was realised by depositing on the samples a solution composed by 94% PEDOT: PSS Clevios PH1000 , 5% Ethylene Glycol (EG), 1% glycidoxypropyl trimethoxylane (GOPS), 0.25% Dodecylbenzene-sulfuric acid (DBSA) (where the volume percentages are referred to the total volume of the solution). EG is a secondary additive that is used to make PEDOT: PSS more conductive. In order to increase the stability of the films in aqueous solution, GOPS, a crosslinker, enhances the creation of covalent connections between the polymer chains. DBSA is a sulfatant utilized to reduce the solution's surface tension, which therefore relaxes more easily on the glass substrate, increasing adhesion. The solution was homogenized and mixed for 10 minutes in an ultrasonic bath. The sample surface was treated with a plasma (parameters: 15 W, 255 Duty ratio, 7 sccm in air for 4 min) in order to clean from resist residues and promote PEDOT:PSS adhesion. The spin-coating method was used to deposit the PEDOT: PSS solution on the slides, using 1000 rpm, t_{dwell} = 30 s and ramp of 1 s. The solution was filtered through a cellulose acetate filter with 1.2 m-diameter pores before being applied to the substrates. The samples were then heated for an hour on a hot plate at 120° C.

- **Step 9: photoresist lift-off**
  After PEDOT:PSS deposition, samples were placed in a container with acetone and immersed for 4 hours and 30 minutes. During lift-off, acetone dissolved the photoresist and, consequently, all the PEDOT:PSS film regions which had been deposited onto it. Samples were then immersed in a new container with fresh acetone and sonicated for 10 s to remove all remaining resist. This procedure was repeated in isopropanol and distilled water. Finally, samples were blowdried with nitrogen flow.

- **Step 10: APTES functionalization**
  Samples were plasma treated (20 W, 255 Duty ratio, 1 min, in air) to introduce hydroxyl groups and therefore facilitating 3-aminopropyltriethoxysilane (APTES) binding. APTES deposition was performed by soaking: samples were in a 5% v/v APTES solution in a 95% ethanol aqueous solution for 1 h. Then, substrates were rinsed carefully with ethanol and distilled water, then dried with a nitrogen flux. Subsequently, the annealing (65 °C for 30 min) was run to crosslink the APTES molecules.

2.2 CA scaffolds methods and characterization

In order to obtain the desired pattern on hydrogels supporting spheroids formation, a series of optimisation and study of the materials chosen were performed. In this section, techniques related to this goal are explored, while the results and final strategy are presented in the next chapter.

2.2.1 Materials and methods

The materials used for scaffolds were alginic acid sodium salt form brown algae by Sigma-Aldrich, crosslinked by calcium chloride anhydrous ($CaCl_2$) by Baker. Both were made in acqueous form by dissolving them in Milli-Q water with concentration of 1.5%(w/V%) for alginate (i.e. 0.015 g in 1 mL of water) and 1 M for calcium solution (i.e. 0.11 g in 1 mL of water).
A commercial AggreWell400Ex plate (STEMCELL Technologies, Canada), which has square pyramidal microwells with 400 μm side length and 250 μm height, was employed as a template to first fabricate polydimethylsiloxane (PDMS) molds. The degassed PDMS precursor mixed with the curing agent (10:1) was poured on the AggreWell400Ex chip and cured at 70 °C for 2 h. The PDMS was peeled off to obtain PDMS molds. Prior to the fabrication of microstructured CA hydrogel, the PDMS mold was treated with O_2 plasma (15 W, 255 Duty ratio, 1 min, air, 7 sccm) to render the surface hydrophilic.
CA hydrogels methods devised were essentially two, shown in Fig.2.1:

- Pouring: a mould was covered by the alginate solution and then the calcium solution was dripped on top of that and left for half an hour in order for Ca^{2+} ions to diffuse and stabilise the network;

- Micromolding: the alginate solution was poured on the substrate of support and the mold is pressed on top of it; right after the system was placed in a calcium bath for half an hour.

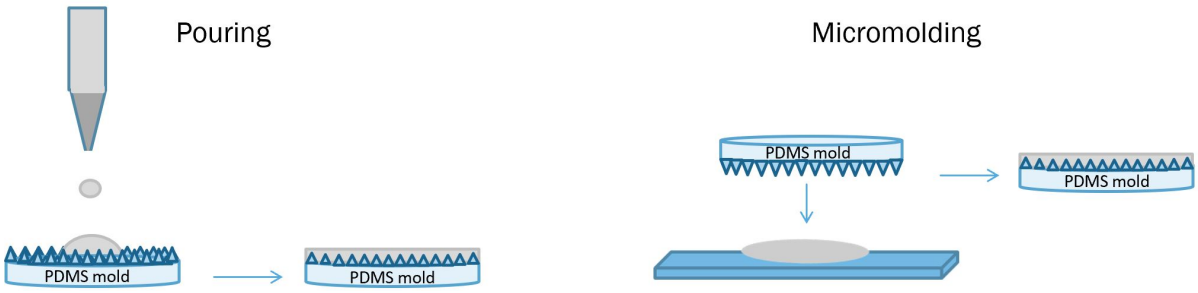

Figure 2.1: Schematic representation of the two possible strategies to prepare CA scaffolds.

2.2.2 Characterization

Thickness estimation

To meet the request of small thickness of the film, which was chosen to be ≤ 350 μm and to attach it to the sensor array substrate, those strategy were tested and improved, as will be described in details in the next chapter. This value of thickness was given to ensure a correct detection of EIS at the bottom of the film, a higher thickness is believed to hamper passage of ions. An estimation of thickness values for each samples was obtained exploiting the microwriter function of telling precisely the thickness in real time as it focus on the sample. By moving along the samples, it was possible to find a mean value and an error.

Structure studies

To understand the properties of CA hydrogel films, also a first study on its structure was performed by means of freeze-drying technique and swelling ratio measures, changing composition of the solution.
Freeze-drying an hydrogel serves to eliminate all the water which swell the structure, leaving the polymeric network and crosslinkings intact. A sample of CA was prepared by simply mixing the two solution into a Florescence flask, then the flask was places for few minutes (around 5- 10 min) into a liquid nitrogen, in order to allow complete solidification. After that, the flask was connecting to a vacuum pump over night and water was removed by sublimation. The sample such prepared was then cut in small pieces and sputtered with a gold layer of around 25 nm thickness, so that it was possible to take good images of the structure with scanning electron microscopy (SEM).
The swelling ratio is defined as the fractional increase in the weight of the hydrogel due to water absorption. Samples were prepared by mixing alginate solution at different concentrations and calcium solution (same concentration at 10 mM) in excess. To measure it, a CA film was left in a petri dish to dry completely over night. Then, it was re-hydrated and it was weighed with the help of a microbalance before and after intervals of time

until it reaches a stable value meaning that the structure is saturated with water. The swelling ratio is given by:

$$SR = \frac{m_t - m_0}{m_0} \tag{2.1}$$

where m_t is the mass at time t and m_0 is the mass of dried hydrogel (i.e. time 0).

Electrical characterization

The last characterization was on CA ionic conductivity. Silverchloride covered silver wires (Ag/AgCl) wires were fabricated and connected to a Keysight B2912A source-measure unit (SMU) in order to provide both the electrodes for the ionic current generation and for voltage measurement. Thus a complete electrochemical cell was prepared, following a similar protocol in [94]. The well is composed of two symmetric parts connected via screw system through a truncated-biconical channel, both of them containing two identical wells to be filled with the solution of interest (Fig2.2). PDMS o-rings of variable diameter

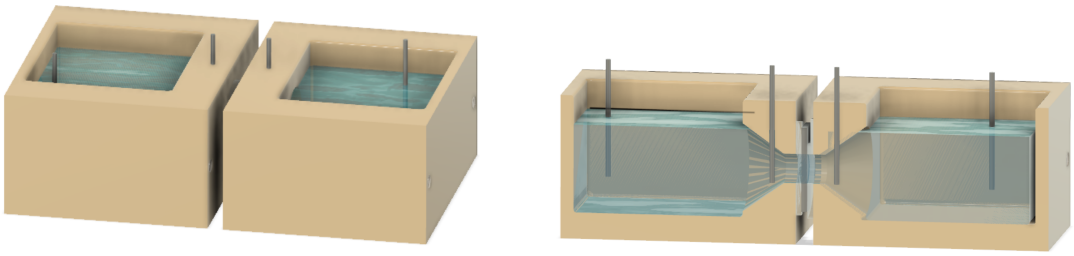

(a) **(b)**

Figure 2.2: 3-D Measurement cell representation in figure (a) and as seen it in section in (b).

were placed in between the two chambers to avoid electrolyte loss and stuck a slice of CA in between. Four Ag/AgCl wires are placed at the ends of the system and connected to the SMU in order to act as electrodes for arbitrarily selected constant currents injection. A 4 point-probe measure was performed. In fact, by using a current source and measuring the potential difference across the channel we can avoid the contribution of potential drops at electrodes due to electrochemical processes always required when a current passes through an electrode. Using the voltage sense technique, we use a high impedance amplifier and hence the current passing through the Ag/AgCl-wire sense electrodes is minimal. Accordingly their potential drop can be neglected. Voltage-current curves was so obtained, from that a resistance is extracted and conductivity can be calculated with Ohm' second law:

$$\sigma = \frac{1}{R} \cdot \frac{L}{S} \tag{2.2}$$

where R is the resistance, L is the length of the sample and S its section.

2.3 Microscopic analysis: AFM and SEM

Optical and electronic investigations on samples played a crucial role in different part of the realization of the device. In the following we briefly introduce the employed techniques used for samples observations, AFM and SEM.

Atomic Force Microscopy

The technique known as atomic force microscopy (AFM) is used to map the topography and examine the characteristics of materials at the nanoscale. AFM interacts with samples material by using a probing tip at one end of a spring-like cantilever (Fig.2.3).

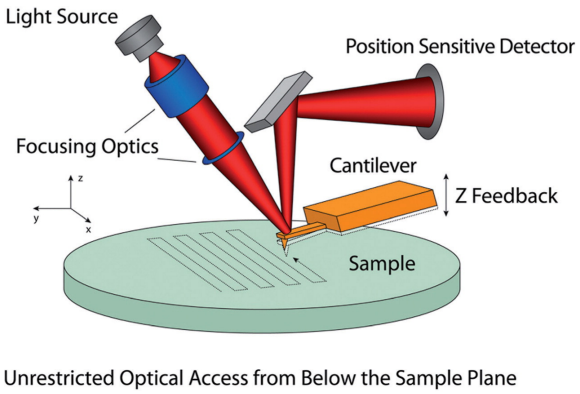

Figure 2.3: Schematic depicting the optical lever detection system used in AFMs. Light is reflected off of the back of a cantilever and read on a detector as the cantilever/probe is raster scanned to measure the topography of the sample. Most of the AFM instrumentation can be located above the sample, allowing for unrestricted optical access from below. Extracted from[95].

There are either attracting or repellent forces produced by the interaction between the sample and the tip, which can reveal details about sample's morphology. Interested readers can find detailed description of atomic force microscopy working principles in [96]. There are two mode of working and below are quickly explained.

NC-AFM fundamentals In Non-Contact Mode AFM the cantilever oscillates at a frequency slightly above its resonance frequency (amplitude <10 nm) in order to obtain an AC signal from the cantilever. The van der Waals force and other long-range forces extending above the surface under investigation cause the cantilever's resonant frequency to diminish (from 1nm to 10nm above it). Instead of touching the surface during scanning, the tip oscillates above it. Because there is very little total force between the tip and sample in this mode, it is perfect for analysing soft or elastic samples (about 10^{-12} N). The cantilever oscillates with an amplitude of a few tens to hundreds of angstroms at or near its resonant frequency (about 100 to 400 kHz). The system senses fluctuations in the resonance frequency or vibration amplitude as the tip approaches the sample

surface. Low force in the non-contact domain makes measurement more challenging than in the contact mode. Cantilevers must also be stiffer in order to prevent being drawn into touch with the sample surface. These factors necessitate the use of a more sensitive AC detection method. The system moves the scanner up and down at each (x,y) data point with the help of feedback in order to maintain a constant resonance frequency and amplitude. Thus, the average tip-to-sample distance is also maintained constant. This scanning action is what creates the data sheet and is utilized to create the topographic image of the sample surface.

c- AFM fundamentals Conductive Atomic Force Microscopy (C-AFM) is a mode of atomic force microscopy in which a conductive tip is scanned in contact with the sample surface, while a voltage is applied between the tip and the sample, generating a current image. A topographic image is also created at the same time. The same region of the sample is used for both the current and topographic images, making it possible to distinguish between surface characteristics that conduct more and less current. The current, which can range from a few pA to 500 nA, is monitored by an electric circuit with amplifiers and filters. The tip may be relocated to a particular desired area after acquiring a topographic image. To create local current against voltage (I-V) curves, the voltage is then increased while the current is being measured.

Scanning electron microscopy

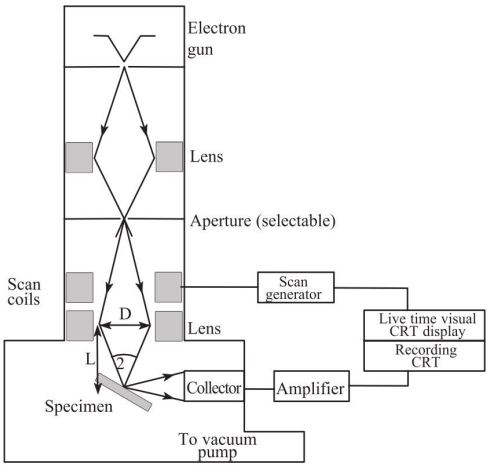

Figure 2.4: Schematic diagram of a scanning electron microscope, from [97].

A focused beam of high-energy electrons is utilised by the scanning electron microscope (SEM) to produce a range of signals at the surface of solid specimens (Fig.2.4). The signals resulting from electron-sample interactions also provide information about morphology, chemical composition, crystalline structure and orientation of its constituent materials. Most often, a portion of the sample's surface is chosen for data collection, and a 2-dimensional picture is created to show the spatial variations. Using typical SEM methods (magnification ranging from 3720X to approximately 30,000X, spatial resolution of 50 to 100 nm), areas with widths of around 1 cm to 5 microns can be scanned in a scanning mode. The SEM is also able to analyse specific point locations on the sample; this method is particularly helpful in detecting chemical compositions (using EDS), crystalline structure, and crystal orientations in a

qualitative or semi-quantitative manner.

SEM fundamentals Significant amounts of kinetic energy are carried by the accelerated electrons in a SEM, and as the incident electrons decelerate in the solid sample, this energy is released as a variety of signals. These signals include heat, photons, visible light, backscattered electrons, secondary electrons, and diffracted backscattered electrons. Commonly used for imaging samples are secondary electrons and backscattered electrons; the former are best for displaying the morphology and topography of materials, while backscattered electrons are best for highlighting variations in composition in multiphase samples (i.e. for rapid phase discrimination). Inelastic collisions between incident electrons and electrons in certain atomic orbitals (shells) in the sample result in the emission of X-rays. The excited electrons produce X-rays with a defined wavelength as they transit back to lower energy states (that is related to the difference in energy levels of electrons in different shells for a given element). As a result, each element in a material that the electron beam "excites" emits distinctive X-rays. SEM examination is regarded as non-destructive since the volume of the sample is not lost due to the x-rays produced by electron interactions, allowing for repeated investigation of the same materials.

2.4 Cell culture method and spheroids growth

The final device was tested using a glyoblastoma cell line, T98G. T98G (CRL-1690™) is a fibroblast-like cell that was isolated from a glioblastoma multiforme, extracted from the brain of a white, 61-year-old, male patient. This cell line was deposited by GH Stein and can be used in neuroscience research. T98G displays a special fusion of typical and altered elements in the regulation of cellular proliferation. T98G cells display the altered traits of anchorage independence and immortality, yet they behave similarly to normal cells in that they become halted in the G1 phase under stationary phase conditions[98]. As a result, T98G cells show that anchorage independence and immortality can both exist, which means that they can overcome the limit of cellular division without becoming senescent and simultaneously without losing the mechanism that distinguish this cell line. The cell line T98G was purchased from ATCC (Manassas, VA, USA) and cultured in Minimum Essential Medium (MEM, Gibco™ 51200046, Thermo Fisher Scientific), supplemented with 10% foetal bovine serum (FBS), 1% L-glutamine, 10% sodium pyruvate and antibiotics (1% penicillin and 1% streptomycin) at 37 °C in 5% CO2 incubator. The cell culture has an indefinite lifespan and a population doubling time (PDT) approximately of 28 h, as reported by the Company. When the cells population reached the sub-confluency (70-80%) was detached by 0.25% trypsin in 0.02% EDTA (both from Merck) solution, re-suspended in fresh Dulbecco's Modified Eagle Medium – Ham's Nutrient Mixture (DMEM/F-12, Gibco) supplemented with 10% FBS and antibiotics (1% penicillin and 1% streptomycin). All chemicals were purchased from Sigma Adrich - Merck KGaA

(Darmstadt, Germany). An aliquot, calculated to have a final density of 0.15 x 106 cells/ml was diluted in 1 ml of supplemented DMEM/F12, as indicated in [99], and plated on the impedance-based biosensor (in the following named h-MEA) previously sterilised by 30 min of 70 % Ethanol. After 30 min from seeding, referred to us as T = 0 h, 2 ml more of medium were added on top in order to fill up the PDMS well measuring Ø 18 mm and deep 10 mm (Fig.3.10). The h-MEA is placed into a small incubator allocated on the motorised translation stage of the optical inverted microscope Eclipse Ti (Nikon, Bologna, Italia). The incubator standard conditions, such as temperature at 37°C and CO_2 concentration at 5%, are guaranteed for up to 72 hours by means of a feedback control driven by a thermocouple and a gas mixer of air/CO_2/humidity (OkoLab Control Unit and Lauda Ecoline 003). The recording section started right 30 min after seeding (T=0h), allowing cells to deposit by gravitation on the CA-Alginate microwells (Fig. X). Phase contrast micrographs of the h-MEA sensing area (1x1 cm, 10 X of magnification) are acquired every 4 hours applying the NIS Elements software Large Images Tool.

2.5 Electrochemical spectroscopy measurements

The set up was constituted mainly by a potentiostat (Autolab PGSTAT 204) connected to the MEA or h-MEA immesersed in a electrolytic solution. It was configured into a three electrode setup consisting of working electrode (a MEA microelectrode), a counter electrode (a platinum wire), and a reference electrode (a Ag/AgCl electrode). Four leads are used to attach the three electrodes to the potentiostat. A working lead and a counter lead are used to carry current, whereas the working sense lead and reference leads are used to sense voltage. This is made by connecting the working electrode to the MEA microelectrode under study, while the counter electrode (CE) and the reference electrode (RE) were placed in direct contact with the electrolyte and the forth lead is massed. Once all leads are connected, the EIS system is setup and ready for testing. The potentiostat generates an AC voltage between the working and the reference electrodes over a wide range of frequencies and gives the possibility to apply an DC offset to the generated AC signal. An integrated frequency response analyzer (FRA) measures the transfer function of the samples and provides their Bode plot, containing the impedance and the phase shift versus the applied signal frequency. The Bode plot can be fitted with the frequency response of an equivalent circuit, providing an electrical modelling of the characterised system.
This set up was used to measure the impedance of microlectrodes without spheroids. For EIS test during spheroid formation a slightly different set up was needed, while the working principles remained the same. First of all, the completed device was placed in a small incubator connected to the optical microscope in order to simultaneously observe it. To connects all pads to the external system, a plastic support containing conducting pins was fixed to the device in a way that each pin corresponded to a pad. Each pin was

also welded to a wire connected to a multiplex (MUX). Then to change the microlectrode under analisis since it was not possible to move the WE manually anymore, the MUX was connected to a Keysight B2912A source-measure unit (SMU), which consented to switch MUX channels. Each channel was connected to a correspondent microelectrode.

Part II

Experimental results

Chapter 3

Fabrication of the h-MEA

3.1 Experimental design and relatives challenges

This project objective is to answers the demanding request of novelty and complementary technologies to exploit in vary research experiments, in order to obtain an insight on cell behaviour when cultured in spheroids.
The idea was to detect spheroids and possibly its growth, trough electrochemical impedance spectroscopy (EIS), combining microfabrication of a sensor multi-electrode array (MEA) integrated with a bio material containing designed cues to direct spheroids growth. Schematically, this is presented in Fig.3.1. The first step was to prepare the two

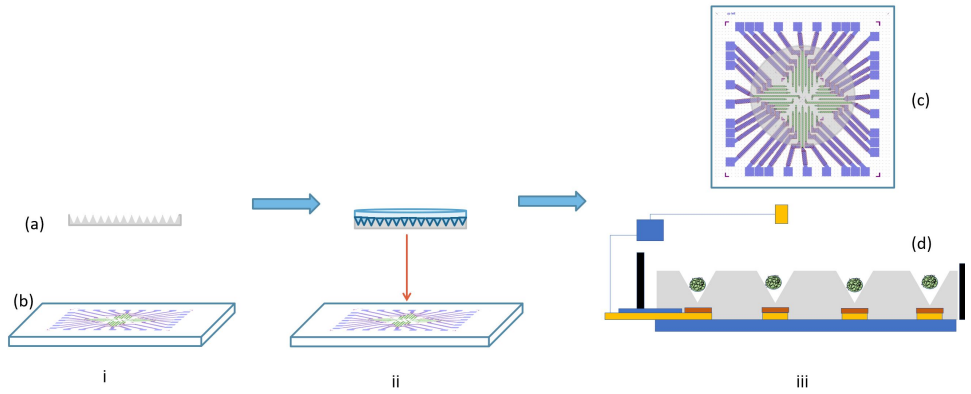

Figure 3.1: Schematic device fabrication. (i) Preparation of (a) calcium alginate scaffold and (b) sensor array on a glass substrate. (ii) Orientation of the scaffold on top of the device so that the wells containing spheroids correspond to sensing electrodes and attachment of the two parts. (iii) Final device: in (c) as seen from above, with coloured parts representing part of the sensor array and the grey area representing the CA scaffold attached, in (d) cross-section view.

fundamental structures, i.e. the sensor array and the biocompatible scaffold. The first one was produced through means of lithography onto a glass substrate, following the step in section 2.1, while the scaffold was made with a film of calcium alginate hydrogel (CA)

patterned with pyramidal microwells. Secondly, those two structures had to be orientated in a way that each well is correspondent to a sensor microelectrode present on the glass substrate and the hydrogel is attached and fixed to it in that configuration. In Fig.3.1(iii) the final device is shown and can be tested by seeding cells and detecting the EIS signal. A glass substrate, represented by the blu layer in Fig.3.1(d), has microelectrodes of gold (in yellow), coated with PEDOT:PSS (in red) which are electrically connected to a multiplexing system for impedance signal recording; on top, a film of CA with pyramidal wells is the substrate where cells can be seeded and this particular 3-dimensional confinement promotes spheroids formation (in this picture represented by green spheres).
For its configuration this device can be defined as a hydrogel assisted multi-electrodes array (h-MEA).
The fabrication and design of h-MEA revealed different challenging aspects:

- finding a reliable standard procedure to produce efficiently CA scaffolds; as seen, ionically crosslinked CA properties depends on a wide range of parameters, mostly uneasy to control in standard working environments.
- The distance between spheroids and sensing microelectrodes must be as short as possible, in order not to screen the signal perturbation (the expected impedance enhancemente) coming form spheroids formation.
- There is a lack of methods in literature to attach CA hydrogel to substrate of different materials, especially in presence of water, as hydrogels contain high amount of it.
- A precise orientation and alignment of the microwells with respect to the microeletrodes is required.

In the following paragraphs, solutions to those problems and the final fabrication strategy are explained.

3.2 Multi-electrode array design and preparation

A customized pattern for the multi-electrode array was developed, with three requirements: (1) micro electrodes had to match the periodicity of wells on the CA scaffolds, (2) the pads that connect each electrode to the external acquiring system had to match the connecting pins, (3) the number of microelectrodes had to be maximised to increase the chances of more number of matches between the two structures. With more electrodes there are more possible wells to monitor, therefore, increase the possibility that a well matching a microelectrode contain a spheroid. In addition, a large number of wells under analysis in simultaneous provide good statistic in an experiment using this device. For those reasons, glass substrates were cut with a diamond tip with dimensions of 50 mm x50 mm and the design drawn accordingly with CleWin4 (a dedicated computer software). In Fig.3.2, it is reported the mask used to produce the device. Precisely, there are 36 circular microelectrodes of three different dimension, i.e. radius of 50, 100 or 200 μm, made of gold coated with PEDOT:PSS to reduce their impedance, in a central area of 10x10 mm (Fig.3.2(b)), which is where micro wells containing spheroids are supposed to be. Each electrode is connected through gold interconnects to external pads. To avoid capacitance effects and detection from unwanted areas each interconnect is isolated with 4um of insulanting material, i.e. mr-DWL5, a negative photoresist purchased by *micro resist technology GmbH*. Other parts present on the mask are functional to orientation of layer during fabrication. The fabrication of such design was achieved, following the procedure exposed in section 2.1.

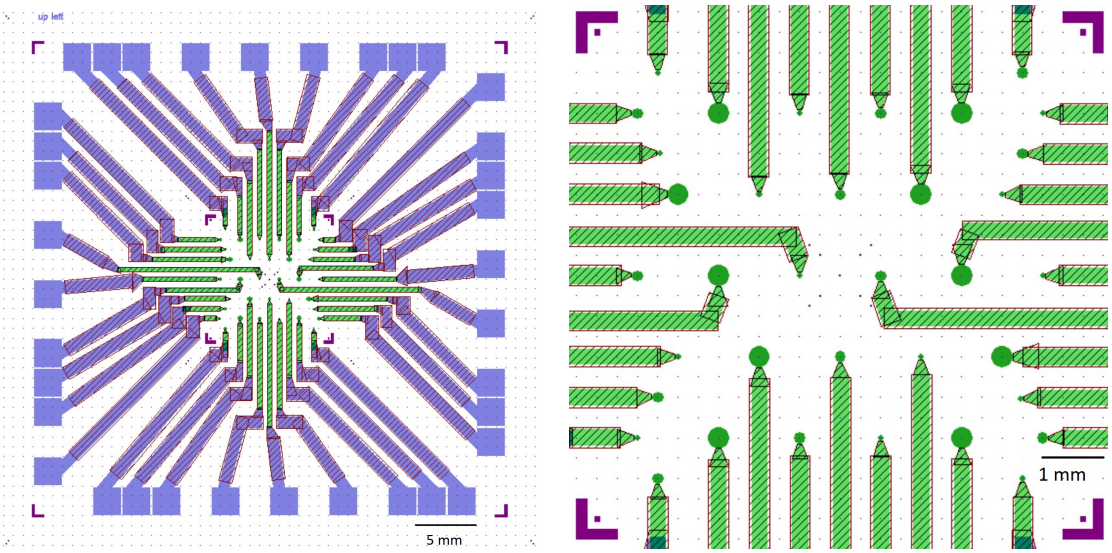

(a) **(b)**

Figure 3.2: Sensor array design as drawn with a specif computer software, CleWin4. In (a) the whole system of wires, pads and microelectrodes are shown and in (b) a selection of the sensing area, comprising 36 microlectrodes.

3.3 Studies on CA structure

Two techniques were used to study calcium alginate structure, swelling ratio test and SEM images of freeze-dried samples[1].

Swelling ratio

The swelling behaviour of physically cross-linked polysaccharides is not fully understood despite its significance in many applications such as drug delivery. Several studies on its variation as function of calcium content can be found in literature, showing that an increase of calcium concentration reduces the degree of swelling [100–102], while it was not known its variation as function of alginate concentration in the constituting solution. To understand how alginate concentration could affect CA structure, three alginate concentration were used forthe solution (%w/V), namely, 10%, 15% and 20% (i.e. respectively 0.010 g, 0.015 g, and 0.020 g of Alg in 1 mL MilliQ water); the concentration of the crosslinker ($CaCl_2$) was fixed at 10 mM (or 0.0011 g $CaCl_2$ in 1 mL MilliQ water) for all these three alginate concentration. In Tab.3.1 are reported the values of masses of 6 samples made with these concentrations (two samples for each concentration) taken before adding water and at progressively over time.

Time [min]	m_1 [g] 10% Alg	m_2 [g] 10% Alg	m_3 [g] 15% Alg	m_4 [g] 15% Alg	m_5 [g] 20% Alg	m_6 [g] 20% Alg
0	0.0112	0.01	0.006	0.0109	0.0056	0.0107
5	0.3696	0.4424	0.2916	0.2916	0.449	0.3973
10	0.5278	0.591	0.5045	0.4951	0.6148	0.6195
15	0.6271	0.8674	0.5491	0.609	0.6979	0.7984
30	0.7032	0.9145	0.5949	0.7649	0.4426	0.9467
45	0.7664	1.0399	0.5789	0.8025	0.4334	0.991
60	0.7341	1.0193	0.5953	0.8091	0.3869	0.9966
90	0.7812	0.9398	0.6058	0.8674	0.5166	0.9637
120	0.7768	0.8982	0.5782	0.8459	/	1.0024
2880 (2 days)	0.8773	0.8411	0.5368	0.8297	/	1.0088

Table 3.1: Measures of masses of 6 samples of CA hydrogels at three concentration of the alginate solution as explicited on the table, fixing the calcium solution concentration at 10 mM. To all values of weight is associated an error of 0.0001 g.

Observing these values, it is possible to note that after 30 min for samples 1,2,3, 4 there's a fluctuation of the weight, meaning that it was not only increasing as expected but it

[1]More details on how these techniques were performed are at section 2.2.

also decreased. An hypothesis of this behaviour could be that samples expressed another phenomenon typical of other food systems, i.e.syneresis [103]. Syneresis is a macroscopic event characterised by a slow time-depended de-swelling of a gel resulting in an exudation of liquid; an example is in milk proteins undergoing sol/gel transition in the course of yoghurt or cheese production. It was proved that CA hydrogels undergoes syneresis [103, 104], but there's very few documentations on this effect.
Additionally, all the samples showed that around 30 min after re-hydratation, an equilibrium is reached and from that moment on there was no consistent increase in weight. A gel swells when a solvent applies an external pressure (also known as a swelling pressure). Due to a balance between two opposing tendencies—the normal increase in entropy from the mixing of the polymer and the solvent and the drop in entropy due to distortion (i.e. expansion) of the network—the swelling pressure equalises to zero at equilibrium [105]. From the values in Tab.3.1, an average swelling ratio at equilibrium was calculated and the results are presented in Tab.3.2.

Although these results cannot be used to outdraw a tendency, probably because the

Sample	Concentrations	Swelling ratio
1	10% Alg, 10 mM $CaCl_2$	68 ± 5
2	10 % Alg, 10 mM $CaCl_2$	93 ± 7
3	15% Alg, 10 mM $CaCl_2$	95 ± 4
4	15% Alg, 10 mM $CaCl_2$	74 ± 3
5	20% Alg, 10 mM $CaCl_2$	78 ± 9
6	20% Alg, 10 mM $CaCl_2$	91± 2

Table 3.2: Average swelling ratio at equilibrium.

difference in concentration was too small to observe a macroscopic effect, the test told which one of those samples could withstand more mechanical deformation. In fact, the test was performed by first extracting manually each sample form the well containing water and then weighting on a microbalance. During this procedure the samples 5 and 6 fragmented in pieces and it was indeed impossible to weight sample 5 after 90 min, while samples 3 and 4 showed less deformation of structure and no fragmentation, which led to chose the concentration of 15% for alginate solution for the preparation of scaffolds.

SEM images

Freeze-drying CA samples it was possible to obtain images of the network characterising this hydrogel. Three samples with the same concentrations used for the swelling ratio test were prepared and the structure is shown in Fig.3.3. The peculiar structure of

CA is well distinguishable in these images: the alginate chains are crosslinked so that they display a network similar to a fishing net. As previus explained[2], ionic crosslinking is a physical crosslinking, meaning that it doesn't involve chemical bonds, but weak interaction between chains and, in this case, ionic bonds between alginate chains are formed thanks to the presence of a divalent cation, i.e. Ca^{2+}.

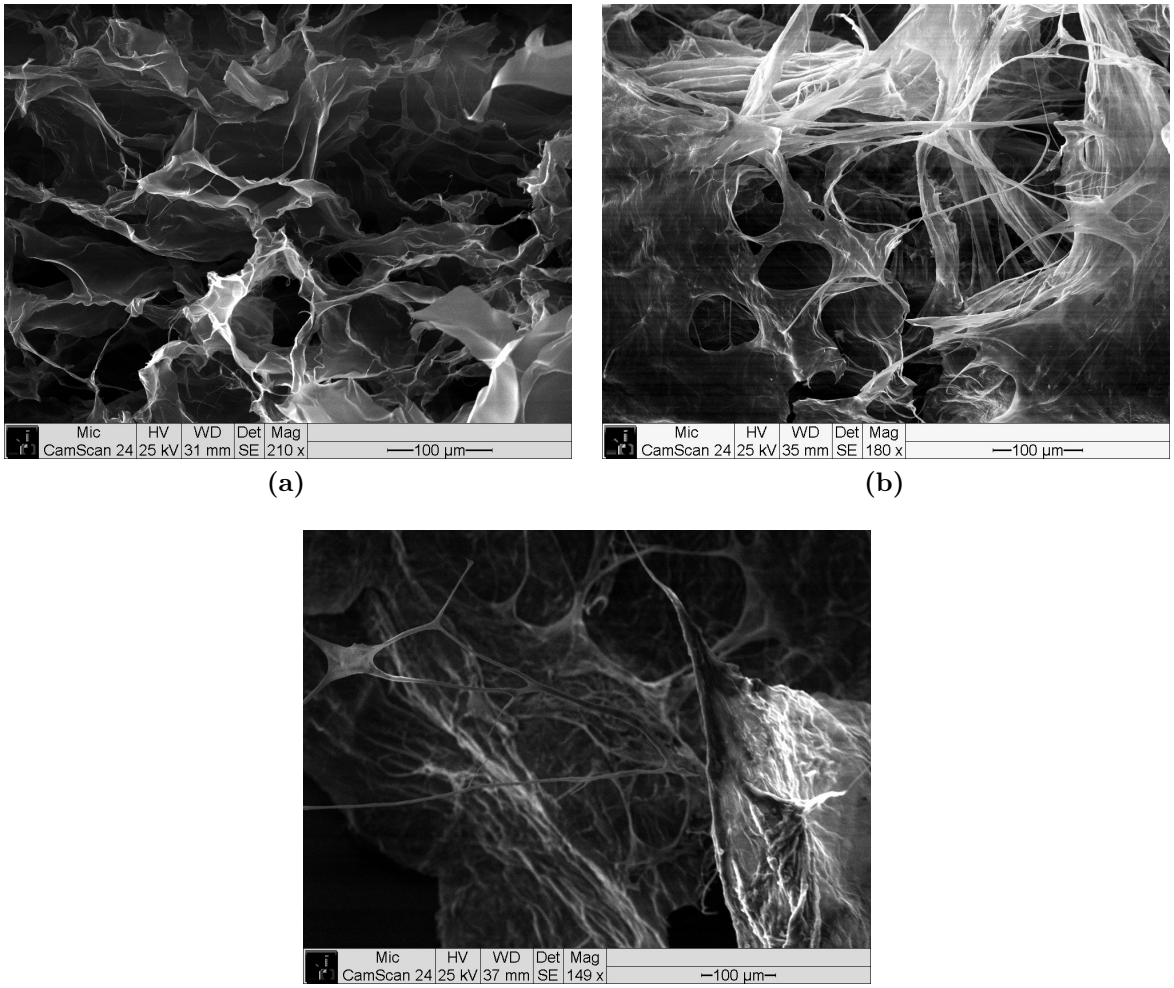

(a) **(b)**

(c)

Figure 3.3: SEM images of CA alginate structure. (a) image shows structure of a sample with concentration 10% Alg and 10 mM $CaCl_2$; in (b) concentration are 15% Alg and 10 mM $CaCl_2$; in (c) concentration are 20% Alg and 10 mM $CaCl_2$.

[2]See section 1.2.2.

3.4 Preparation methods for CA scaffolds

As seen in section 2.2, two methods were found to realise CA scaffolds, which needed an optimisation to obtain a suitable one for this specific device fabrication.

3.4.1 Optimisation of methods

Ionic cross-linking between multivalent cations and alginate takes place instantaneously and therefore molded hydrogel are not easily prepared by combining these two ingredients together directly, as they tend to create lumps or areas of different rate of crosslinking, which in turn effects homogeneity. Thus, it was necessary to do several attempts to prepare CA scaffolds able to maintain the pattern along all the surface.
A commercial AggreWell400Ex plate containing pyramid-shaped microwells was used as template for patterning CA hydrogels. As shown in Fig.3.4, PDMS molds fabricated from the AggreWell400Ex plate consist of a high-density array of square-pyramids with about 400 μm width and 250 μm height.

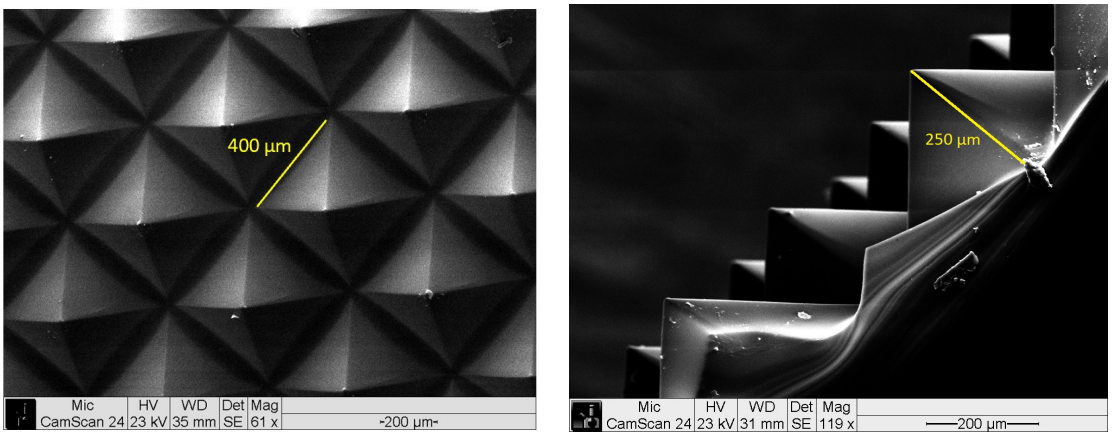

(a) **(b)**

Figure 3.4: SEM images of PDMS molds used as template for CA scaffolds.

Molded CA hydrogels were prepared from this template using both strategies exposed in section 2.2, with solution concentrations of 15% alginate and 10 mM $CaCl_2$, followed by a drying treatment to remove water. The morphology of the microstructured CA hydrogel was analysed using optical microscopy and scanning electron microscope of samples sputtered with gold (in Fig.3.5). The corresponding microstructured CA hydrogel was composed of square-pyramidal wells, although the pattern was not always perfectly following the template, since some areas presented the right shape of wells and others presented partially formed or not formed at all wells, as demonstrated by the images in Fig.3.5. Several attempts were carried out, using either pouring or micromolding

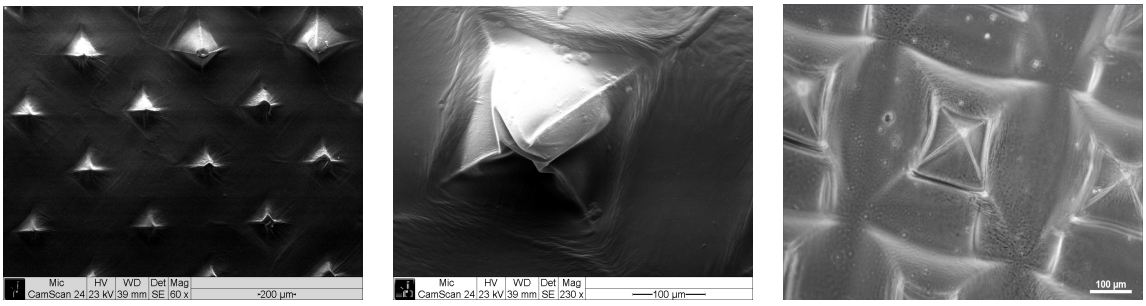

(a) **(b)** **(c)**

Figure 3.5: Images of molded CA hydrogel, seen at SEM (a) and (b), and observed at the optical microscope (c).These samples were prepared by micromolding with concentration of 15% Alg and 10mM $CaCL_2$, dried under the fumehood overnight.

methods and changing gelation parameters, such us temperature of gelation, drying method, concentration of solutions, but all samples showed similar structures as in Fig3.5.

The problem was connected with the dehydration of the CA scaffold: our hypothesis is that drying this hydrogel causes an excessive shrinkage of the structure which can no longer maintain the molded pattern. Indeed, successful results were finally obtained by skipping the step of drying, as shown in Fig3.6. The concentration chosen were: 15% alginate and 1 M $CaCl_2$. As previously explained (section 1.2.2), increasing the calcium content in CA hydrogels leads to a stiffer structure and for this reason the calcium solution concentration was raised from 10 mM to 1 M, rendering CA scaffolds self-standing. In Fig.3.6, it is reported the optical images of CA scaffolds, realised with micromolding in (a) and pouring technique in (b).

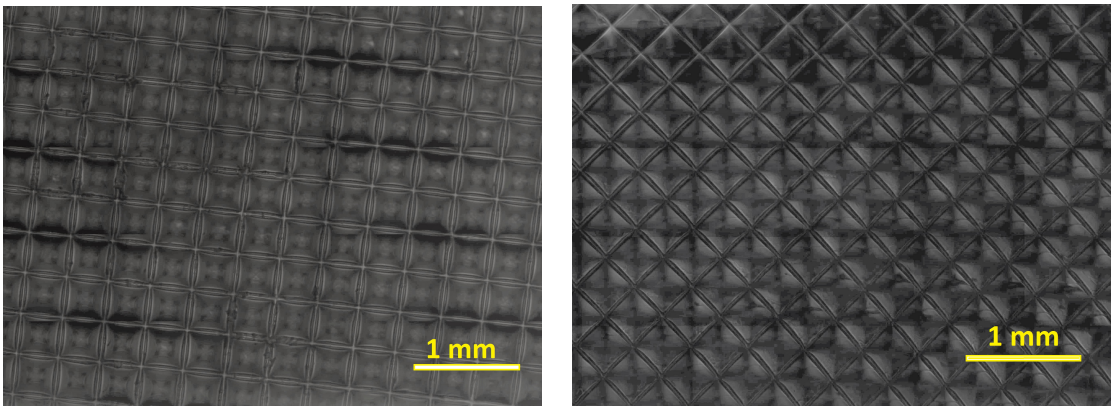

(a) **(b)**

Figure 3.6: Images of CA scaffolds at optical microscope. In (a) CA is obtained with micromolding and in (b) with pouring.

These two techniques are both reliable and give the perfect reversed structure of the PDMS mold on CA hydrogels. The only difference that was detected was an increase of roughness on the face not patterned of the hydrogel, using the pouring technique. Since calcium solution was dripped on top of the layer of alginate solution covering the mold, in the point of contact between the two solution the gelation is instantaneous and creates ridges. Instead, with micromolding the interaction between alginate chains and calcium ions depends on diffusion from a large outer reservoir into an alginate solution, which is therefore slower. Another explanation of the unseen ridges on other face is that the support substrate plays also the role of a mold for that surface.

Thickness estimation

To ensure a correct detection of spheroids, the distance between them and microelectrodes underneath was made as short as possible, which consequently means that CA scaffolds thickness had to be reduced. Considering that the PDMS mold height is of 250 μm, maximum hydrogel thickness of 350 μm was considered acceptable for this purpose. Two concentrations for the alginate solution were used, i.e 1.5% and 5% in %w/V, in order to create even more stiffer scaffolds. The results are shown in Tab.3.3, together with the strategy of production.

Sample name	Concentrations	Amounts (Alg+ $CaCl_2$)	Surface area [mm^2]	Methods details	Thickness [µm]
Micro1.5%+1M_1+2_958	15% Alg 1 M $CaCl_2$	1 +2 mL	958	Micro-molding	716 ±50
Pour1.5%+1M_1+2_958	1.5% Alg 1M $CaCl_2$	1+ 2 mL	958	Pour	690 ± 70
Micro1.5%+1M_0.5_958	1.5% Alg 1M $CaCl_2$	0.5 mL + $CaCl_2$ bath	958	Micro-molding	488 ± 25
Pour1.5%+1M_0.5_958	5% Alg 1M $CaCl_2$	0.5 mL+ $CaCl_2$ bath	958	Pour	446 ± 65
Spin1.5%+1M_0.5_958	1.5% Alg 1M $CaCl_2$	0.5 mL + $CaCl_2$ bath	958	Spin 30s 500 rpm	350 ± 70
Spin5%+1M_0.5_958_1000rpm	5% Alg 1 M $CaCl_2$	0.5 mL+ $CaCl_2$ bath	958	Spin 30s 1000 rpm	282 ± 60
Spin5%+1M_0.5_958_500rpm	5% Alg 1M $CaCl_2$	0.5 mL + $CaCl_2$ bath	958	Spin 30s 500 rpm	350 ± 45
Spin1.5%+1M_0.2_254_500rpm	1.5% Alg 1M $CaCl_2$	0.2 mL + $CaCl_2$ bath	254	Spin 30s 500 rpm	345 ± 44
Spin1.5%+1M_0.2_254_500rpm_2	1.5% Alg 1M $CaCl_2$	0.2 ml + $CaCl_2$ bath	254	Spin 30s 500 rpm	326 ± 40

Table 3.3: Thickness values of CA scaffolds. Sample names directly report the main details of production, which are also clarified in the Table: concentrations of solutions, amount of solutions used, mold surface area and method used.

Based on experience in producing CA scaffolds, the thickness depends on the amount of material used respect to the surface area: using greater volume of alginate solution on the same surface dimension leads to higher thicknesses, while decreasing the volume or

increasing the surface area reduces the thickness. To reach the chosen thickness value, a series of test were made. The results shows that (1) both pouring and micromolding techniques give similar thickness values, (2) increasing the content of calcium does not increase the thickness, (3) it is possible to mold CA hydrogels into desired thickness and shape, with different concentrations of alginate solution.
On the other hand, covering the PDMS mold with 5% alginate solution was not an easy task (especially with low amounts), due to the high viscosity of the solution. Therefore, to spread it evenly, the solution was spin-coated on the PDMS mold, proceeding then either with pouring or micromolding technique which gave same thickness values. Spin-coating was also used for reducing the thickness of samples made with 1.5% alginate solution. To meet the requirement of fitting the CA scaffold in a well, small enough to be inserted inside the plastic support used to connect the h-MEA to the EIS acquiring system, the mold area was reduced by cutting with a puncher the mold into a cylinder of surface 254 mm^2. Strategies valid for this other area dimension were found and the details are shown in the table.
As can be noted, for both alginate concentrations and mold areas, it was possible to achieve a good procedure to prepare perfectly patterned CA scaffold with thickness around 350 μm, but, since the alginate solution at 1.5 % was less viscous and easier to handle, was selected as the more suitable concentration.
The final strategy parameters hence are:

- **Concentrations** for alginate solution 0.015 Alg in 1 mL MilliQ water and for calcium solution 1.1 g $CaCl_2$ in 1 mL MilliQ water (i.e. 15% Alg and 1 M $CaCl_2$)
- **Spin coating parametrs** 500 rpm, t_{ramp} = 1 s and t_{dwell} = 30

3.5 Orientation and fixing of the CA scaffold and the MEA

The problem of attaching a CA scaffold to a MEA was crucial in the realisation of the h-MEA: if the CA scaffold is not attached to the MEA, there is no microlectrode-well orientation and the distance between spheroids and microelectrodes is not controllable, since CA hydrogels tipycally float in cell culture media. It was exploited the ability of sodium alginate to create a bound with 3-aminopropyltriethoxysilane (APTES). In fact, in literature there are few examples of preparation of membranes or beads by combination of this two materials[106–108], but none used for sticking a CA hydrogel to a surface. Therefore, the method of preparing CA scaffolds needed to address also this problem, which means that a reverse micromolding technique was chosen as strategy since it could secure a direct interaction between sodium alginate and APTES (the MEA surface was functionalized with APTES, as reported in 2.1).

To orientate CA scaffold on top of the MEA, the set up in Fig.3.7 was arranged: attached to an optical microscope, there is an elevator with a customised metallic extension at which is fixed a support able to rotate on the plane. The MEA is affixed at the rotating support, while the PDMS mold covered with alginate solution is affixed to the microscope stage. Hence, the PDMS mold can move along x and y direction, while the MEA can rotate on the plane and move along z direction.
In Fig.3.8, it is reported how the two structures appear looking through the microscope when orientated. As seen, each microelectrode corresponds to a well on the CA scaffold.

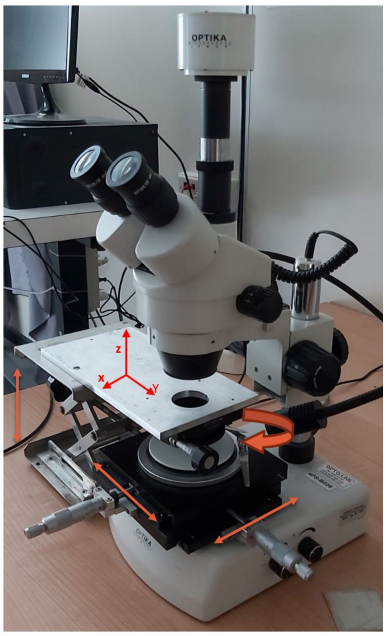

Figure 3.7: Set up of orientation.

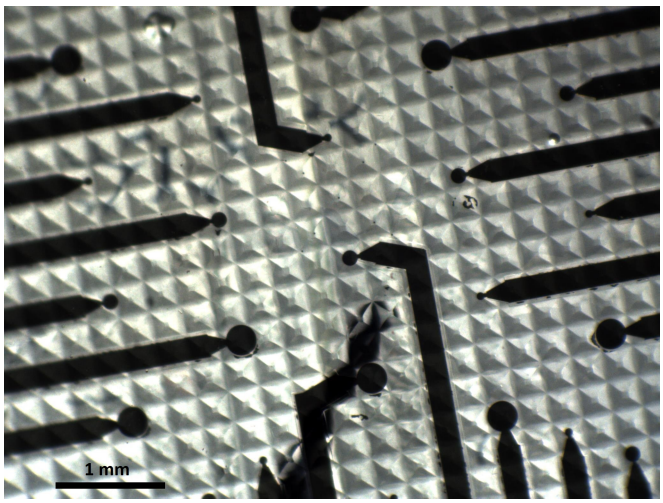

Figure 3.8: Optical image of the MEA orientated on the top of the CA scaffold.

3.6 Summary of the fabrication procedure for the h-MEA

The procedure to fabricate of the h-MEA, under the developments discussed in the last sections can be, as follow, synthesised.

1. **Fabrication of the MEA**, following the steps explained in section 2.1, the design shown in Fig.3.2 is realised.

2. **Fabrication of a CA scaffold and orientation of the two structures**: As seen in the previous section, the CA preparation strategy has to be adjusted in order to create a bound between the alginate solution and APTES, present on the MEA surface. The procedure is sketched in Fig.3.9. First, sodium alginate solution (with concentration of 1.5%) is poured on top of a mold, then the solution is spread evenly by spin-coating (500 rpm, 30s dwell, 1s ramp). Finally, the two structures are orientated one respect to each other and all the system is left in a bath of $CaCl_2$ solution for half an hour to ensure a complete crosslinking. In this way, the CA scaffold preparation follows a reverse micromolding strategy.

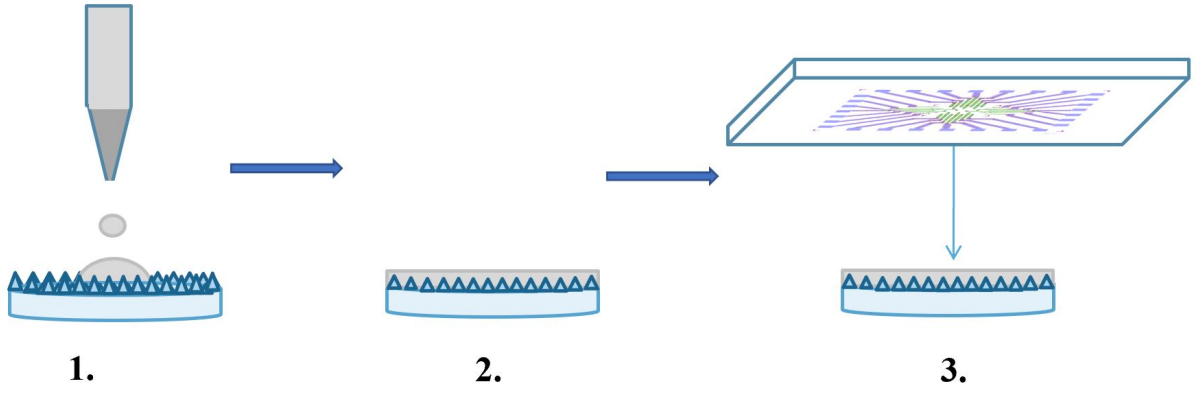

Figure 3.9: Steps of reverse micromolding technique to prepare h-MEA. 1. sodium alginate is poured on top of a mold, 2. spincoating of sodium alginate, 3. orientation and attachment to the MEA.

3. **PDMS well preparation**: In order to confine cell culture medium on top of the CA scaffold without short-cut on the MEA, a PDMS cylinder with an hollow central part of the dimension of the scaffold is glued to the glass substrate.

In Fig.3.10, a picture of the final device obtained following this procedure is presented.

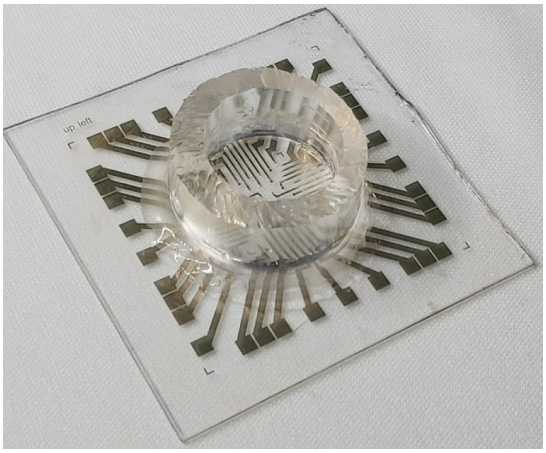

(a)

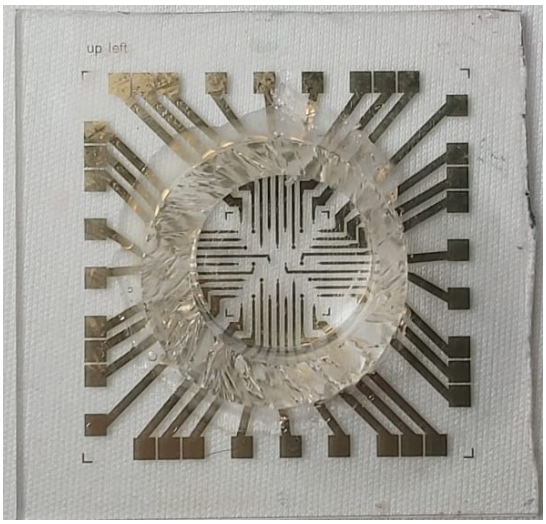

(b)

Figure 3.10: Pictures of a complete h-MEA, in (a) from one side and in (b) as seen from the top.

Chapter 4

Testing and characterisation of the h-MEA

4.1 Calcium alginate ionic conductivity

Due to the device configuration, assessing the electrical behaviour of CA scaffold is important to understand the effect of the presence of the hydrogel on EIS spectra. A good conductivity, indeed, would secure also a good measure of impedance given by spheroids. The set up explained in section 2.2.2 was used to obtain V-I characteristics of two CA cylinders, made with 5% and 1.5% alginate solution crosslinked with the same calcium solution (1 M $CaCl_2$). Looking to the experimental set up, the conductivity derived from such measures is the one of the cylinder between the two sensing electrode in Fig.4.1. The CA alginate slices were put between these two wells, containing the spheroids culture

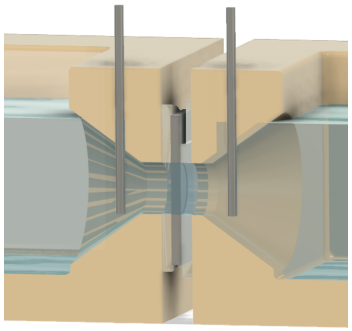

Figure 4.1: Detail on the experimental set up.

medium in order to detect how CA could hinder/allow the passages of the same ions used in the real experiment.
The feature of the cylinder under analysis are presented in Tab.4.1 for each test performed.

Test	Length [mm]	Cross section [mm^2]
Blank	16.45 ± 0.05	19.63 ± 0.8
1.5% calcium alginate	16.61 ± 0.05	19.63 ± 0.8
5% calcium alginate	17.40 ± 0.05	19.63 ± 0.8

Table 4.1: Specifics of dimensions of cylinder analysed through ionic resistance measurements.

The V-I graphs are shown in Fig.4.2. The current sweeps from -1 mA to 1 mA between the two external electrodes, while the two internal electrodes register the voltage produced. Two mean time of measurements (1 s and 5 s) are selected to observe any changing if the sweep in current is slower or faster. It was found that both the two samples do not show any hystereis at both mean time and present an high conductivity. The slopes extracted from these graphs give the values of resistance to the ionic flow and from that the ionic conductivity can be calculated. The values are listed in Tab.4.2.

Test	Resistance [Ω]	Ionic conductivity [S/m]
Blank	268.7 ± 0.18	3.11 ± 0.09
1.5% calcium alginate	273.89 ± 0.35	3.09 ± 0.09
5% calcium alginate	298.98 ± 0.07	2.96 ± 0.08

Table 4.2: Values of resistance and conductivity for Blank- spheroids culture medium, 1.5% calcium alginate and 5% calcium alginate. Error associated are of 3%.

The value of conductivity found for the cell cultre medium (DMEM/F12, supplemented with FBS and P/S) is comparable to the value found in literature [109, 110] of around 1.7-1.8 S/m. The difference depends on the different concentrations used for FBS, which increase the salt ions concentration. Furthermore, the approximation of the sample volume to a cylinder could change slightly the real value.
The calcium alginate is perfectly conductive and acts as a salt bridge or ion bridge: the conductivity does not decrease if a layer of calcium alginate is put in between the ion flow, but it can allow ions to jump from one well to the other with a very low increase in resistance. The lower concentration of alginate brings higher values on conductivity, which makes the 1.5% concentration more favourable to prepare the h-MEA. The electrical behaviour of calcium alginate exhibit characteristic differences attributed to the hydrogel structure and ion concentration of solution, therefore a direct confront with literature was not found for this particular combination.

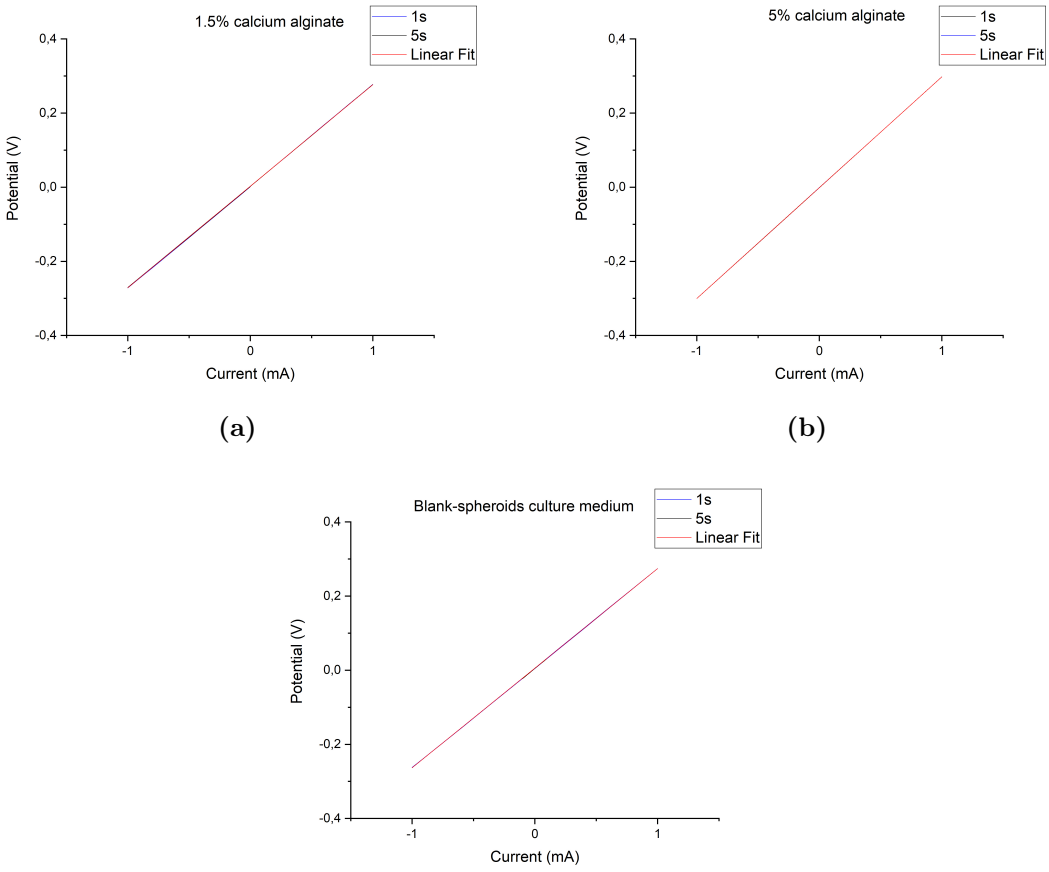

Figure 4.2: I-V characteristics taken with 4PP technique for (a) 1.5% calcium alginate; (b) 5% calcium alginate; (c) Blank test, i.e. with spheroids culture medium. The two mean time used (1 s e 5 s) and fits perfectly overlay.

4.2 Electrochemical impedance characterisation

In this section are reported the electrochemical impedance spectra for the device fabricated. First, it was studied the impedance given by the MEA, then the same test was performed on the same device with the alginate attached to the MEA (i.e. to the h-MEA) to see the change in the shape given by the presence of the alginate. For both tests, the electrolyte solution used was a 1X PBS.
To make easier to understand which microelectrode is associated to the specific curve in the next graphs, Fig.4.3 shows the number associated to each microelectrode on the design pattern.

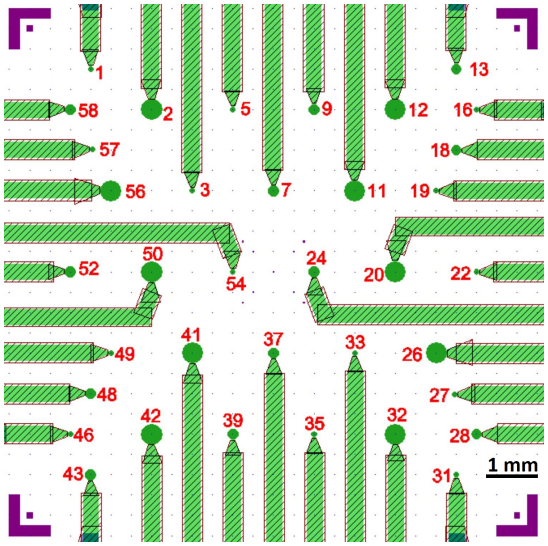

Figure 4.3: Index of microelectrode on MEA.

4.2.1 EIS spectra of MEA

In Fig4.4 are reported the best Bode plots according to the microelectrode dimension (50, 100 and 200 radius). Each plot depicts the acquired impedance and phase in function of the input signal frequency. The transfer function of the PEDOT:PSS coated microelectrodes is fitted using a simple R(RC) equivalent circuit model, in Fig.4.4(b). A flat impedance response (with phase 0) is observed in the high frequency range, which corresponds to the electrolyte resistance R_el. Moving towards lower impedances, | Z | increases according to the capacitive behaviour of the electrode, that is determined by the ionic double layer (C_dl) at the interface. The presence of the conducting polymer layer affects the impedance, that decreases more than an order of magnitude in the capacitive regime, thus leading to a wider frequency range for the flat impedance response. Noteworthy, a flat response is reached in the range 100 Hz – 3 kHz, which is interesting

for bioelectronic recordings and stimula. This impedance drop is related to the switching from a 2D metallic interface to a 3D polymeric one, together with the introduction of ionic conduction (in addition to the standard electronic one, present in metals).

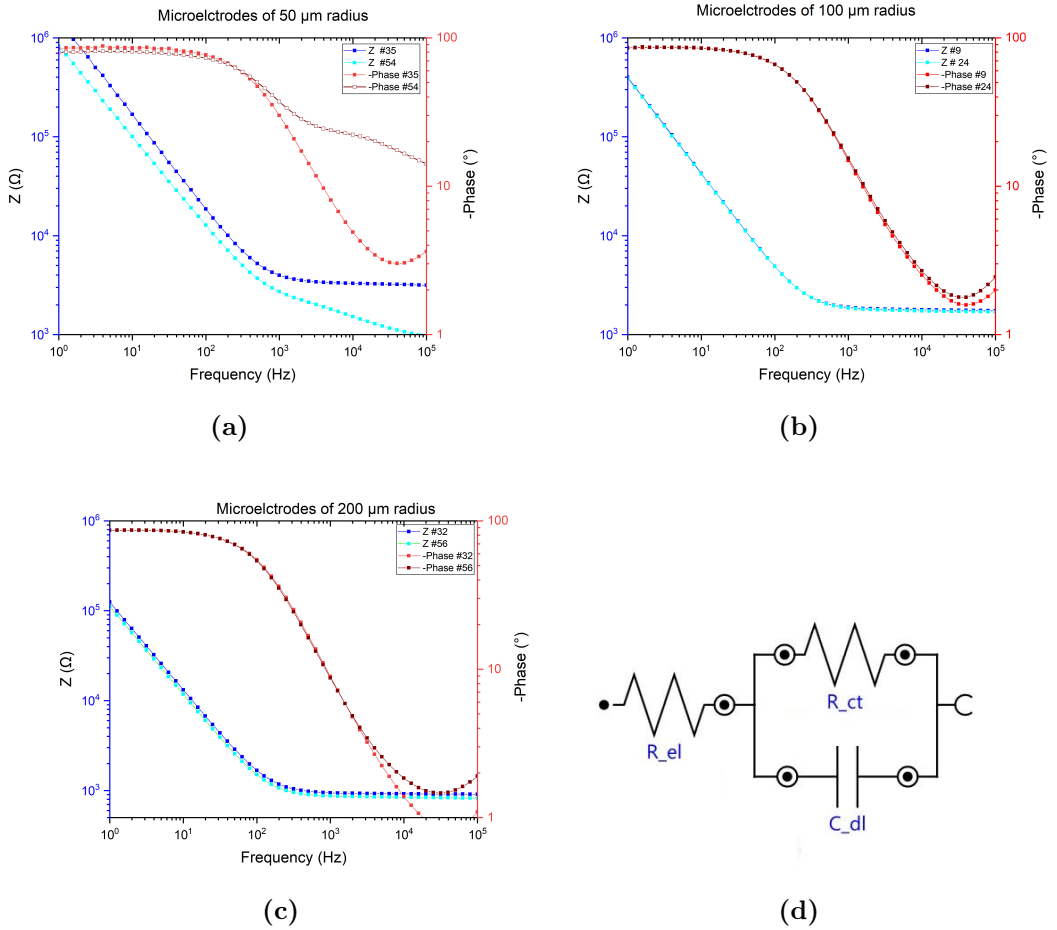

Figure 4.4: EIS spectra, reporting phase and |Z|, measured from a MEA for microlectrodes of 50 μm in (a), 100 μm in (b), 200 μm and in (d) the model circuit used for fitting. Different colours represent the spectrum for different electrodes indicated with a number. The blue and cyan lines always indicate Z, while red and wine the phase for each electrode.

It was observed also that the impedance and particularly the shape of the phase curve change greatly and this behaviour, together with rupture behaviour, was registered for all electrodes with different occurrences (12 over 14 for 50 μm radius, 5 over 12 for 100 μm radius and 3 over 10 for 200 μm radius). The reasons of this trend could be linked to a problem with the coated layer of PEDOT:PSS or to random failures during fabrication of other part of the MEA.
It is believed that some electrodes show sign of partial or total delamination of PEDOT:PSS, as already reported [111]. Delamination is considered to be mostly a con-

sequence of poor material binding between the conducting polymer and underlying substrate[112] and therefore, physical and chemical means of adhesion are recommended. In our case, we have used GOPS as a cross-linker of the PEDOT:PSS and to help with substrate adhesion; although, it is not expected that there is chemical bonding between this polymer and metal. This affects majorly electrodes of 50 μm because the lift off process is aggressive and create micro cracks on the surface, which in proportion effect much more a smaller area.
Fitting the plots with the model in Fig.4.4(d), it's possible to extract the value of capacitance linked to the formation of a double layer at the PEDOT:PSS interface, which can be therefore considered as the PEDOT:PSS capacitance. A mean value for PEDOT:PSS volumeric capacitance were calculated according to dimension:

- C/V= 32 $\pm$ 5 F/cm^2 for microlectrodes of 50 μm radius;
- C/V = 38 $\pm$ 4 F/cm^2 for microlectrodes of 100 μm radius;
- C/V = 33 $\pm$ 3 F/cm^2 for microlectrodes of 200 μm radius.

The volume is given simply by the cylinder of PEDOT:PSS covering the electrode. The radius dimensions are known, while the thickness were measured with a NC-AFM and the mean value is 320$\pm$ 20 nm. These values are comparable to standard C/V values for PEDOT:PSS [113].
Comparing the data of different dimension electrodes, what can be noted is that increasing the radius the capacitive behaviour sets for lower frequencies. The phase response never starts precisely on 0° due to the non ideality of the system.

4.2.2 EIS spectra of h-MEA

The aim of these tests performed on the same device was to clarify if the CA hydrogel can change the impedance and phase response of the MEA.
The plots of EIS are shown in Fig.4.5. According with the previous results, the electrodes of 50 mum are those displaying most delamination signs. Indeed, delamination is also more likely in successive measures, as well as swelling of of PEDOT:PSS which can damage the film.
Differently, for microelectrodes of 100 and 200 μm stable impedances or marginal increases (<10%) has been recorded. Hence, the fitting was performed with the same Randles model.
The mean values of C/A are very similar to ones for MEA, apart for 50 μm electrode, which, as already discussed, were mostly damaged:

- C/V= 8 $\pm$ 1 F/cm^2 for microlectrodes of 50 μm radius;
- C/V = 38 $\pm$ 4 F/cm^2 for microlectrodes of 100 μm radius;

- C/V = 26 ± 3 F/cm^2 for microlectrodes of 200 μm radius.

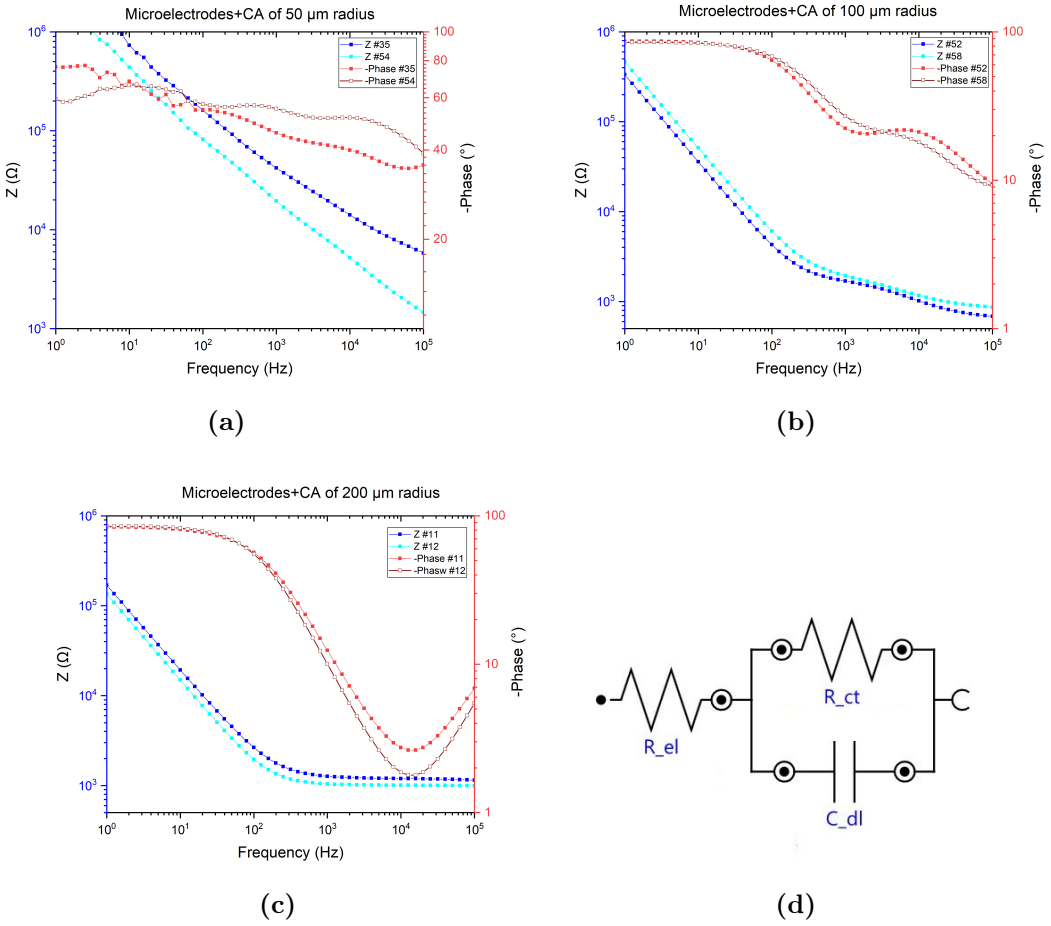

Figure 4.5: EIS spectra, reporting phase and |Z|, measured from a h-MEA for microlectrodes of 50μm in (a), 100 μm in (b), 200 μm and in (d) the model circuit used for fitting. Different colours represent the spectrum for different electrodes indicated with a number. The blue and cyan lines always indicate Z, while red and wine the phase for each electrode.

4.3 h-MEA testing for spheroids growth

Ultimately , the h-MEA was tested for detection the formation of spheroids of the T98G cell lines.
Following the procedure in section 2.5, the cell were seeded on top of the h-MEA and the culture was monitored for 4 h, optically and electrically.
In the following, it is reported a selected result. Among the 100 and 200 μm radii electrodes, which were found to be the most reliable in keeping the C/V ratio stable for all subsequent measurements, the recording area of number 7, which has radius of 100 μm (Fig. 4.1), was a perfect match for the cells and their respective CA microwell.
The results are presented in Fig.4.6. These plots show impedance and phase as changing

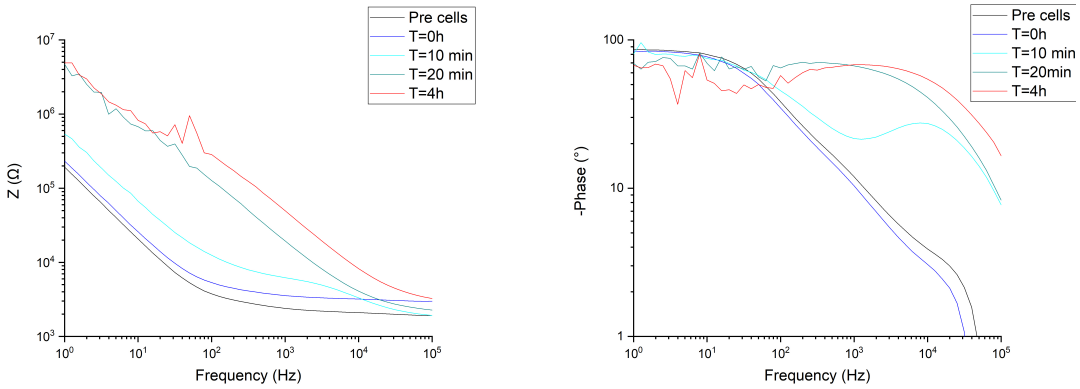

(a) **(b)**

Figure 4.6: EIS spectra given by monitoring spheroids formation. Each curve represent the values of impedance at different 5 times in (a) and in (b) the values of phase registered simultaneously.

in time for the same electrode and can sharply unveil an increase in impedance and phase, due to first the presence of cells and then the starting of formation of a spheroid at T=4. In the following, each time is analysed separately.

Before seeding

The electrode presents the typical characteristic impedance and phase of the h-MEA before the seeding of cells, as shown in Fig.4.7(a), which can be fitted with a simple circuit model depicted in Fig.4.7(b) with the value used. It's important to note that a slightly difference is due to the different electrolyte used in the previous test on h-MEA, which was 1X PBS while in this plot is the cell culture medium, i.e. DMEM/F12, supplemented with FBS and P/S

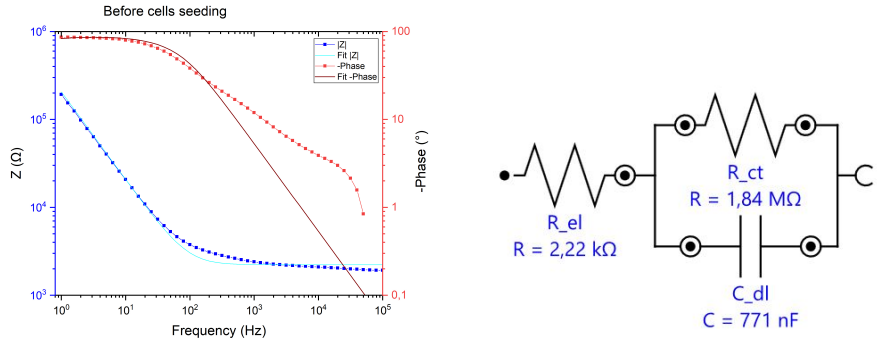

(a) **(b)**

Figure 4.7: EIS spectrum recorded before seeding cells in the same electrolyte. The blue and cyan lines indicate Z and its fitting, while red and wine the phase and its fitting.

T= 0h, T= 10 min and T= 20 min

The cells were, hence, seeded on top of this device and after 30 min (T= 0h) it was possible to appreciate that they were trapped at the bottom of the well, in Fig.4.8.

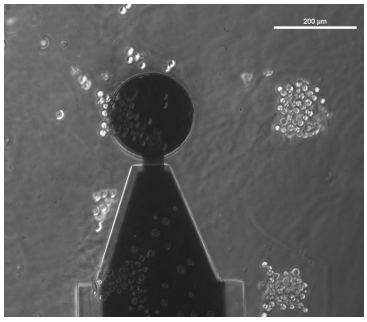

Figure 4.8: Optical image of the electrode under analysis covered with cells, that are deposited at the bottom of the CA microwell present (not visible).

By monitoring electrochemically the system along these time points, it was noted a

change of the curves shape of impedance and phase correlated to the cells accumulation. In Fig.4.9 are shown in details this behaviour, alongside with the relative circuit model that was found fitted the curves the best. As expected theoretically, the model circuit

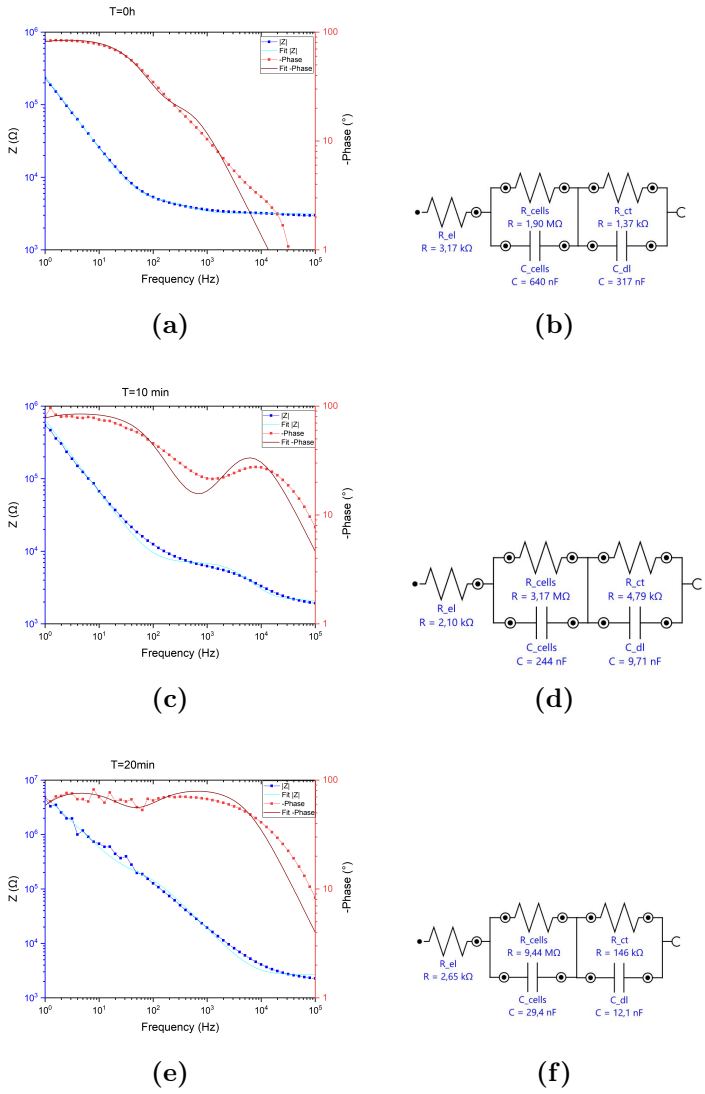

Figure 4.9: EIS spectra, showing impedance, in blue and cyan, and phase, in red and wine, at time T=0 h in (a) with its corresponding circuit for fitting that display values of fitting in (b); in (c) at T=10 min and corresponding fitting circuit in (d) and in (e) for T=20 min with its corresponding fitting circuit in (f).

able to represent this new system is composed by two RC elements, the capacitance and resistance associated to the cells and the capacitance and resistance associated to the electrode connected to it. This is also suggested by the presence of two peaks more or less evident on the phase function. Another difference is notated on the value of impedance: the range is indeed shifted to high values ($1 \cdot 10^3$ to $1 \cdot 10^7$) as reaching the 20 min after

cell deposition.

T=4h

Lastly, after 4 hours the cells were starting self organising in an unique agglomeration as shown in Fig.4.10.

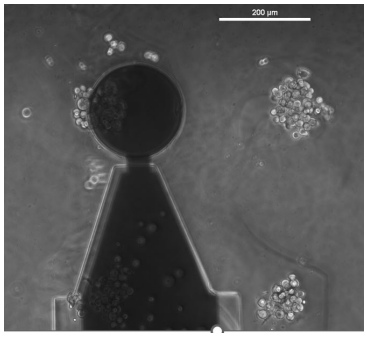

Figure 4.10: Optical images of the electrode covered with cells after 4 h of seeding.

In the Fig.4.11 are reported the impedance and phase plot and its relative circuit model. It is evident the trend of increasing impedance values in addition to a well fitted plot as

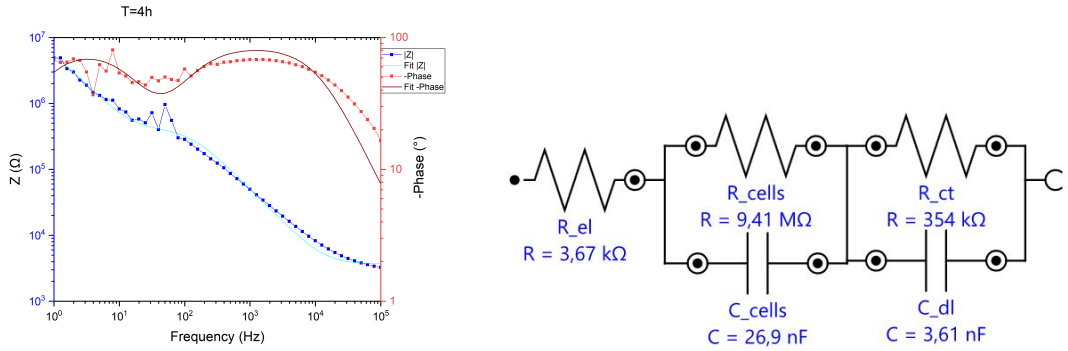

(a) **(b)**

Figure 4.11: EIS spectra of impedance in blue and light cyan, and phase, in red and wine, at time T=4 in (a) and the model circuit used for fitting, which show also values of fitting used.

a two RC elements. Thus, an expected outcome continuing monitoring over time is an increase in impedance until a stable state corresponding to the complete formation of spheroids (so after 24 h).
These preliminar results proves the applicability of the device to studies with interest in monitor growth of spheroids, as well as detection of them.

Conclusion

3D cell cultures have revolutionised our understanding of cellular behaviour, both in vivo and in vitro, expressing their potentiality for a wide type of experiments in different fields of Science, such as drug delivery and testing, cancer studies, tissue engineering and bioengineering more broadly. Notwithstanding five decades of technology and engineering since the first exploration of the differences between cells grown on a flat surface versus three-dimensional formats[114] have passed, there is still a lack of suitable technologies to survey continuously these systems without damaging the sample. Recently, a new route has been open with label-free electrochemical impedance sensors, which are able to detect a variety of biological variables and processes, with the benefits of being non-invasive and reasonably priced [17]. In this contest, my thesis work presents a novel device to study in real time spheroids formation.

The biosensor produced, named h-MEA, is based on a multi-electrode array (MEA), composed of 36 microelectrodes of 3 dimensions (50 μm, 100 μm and 200 μm radius) made in gold coated with PEDOT:PSS, to which is attached a calcium alginate (CA) scaffold supporting the growth of spheroids, a type of 3D cell culture format. It was idealise and proved a new fabrication technique for efficiently fabrication of these scaffold with defined thickness and surface area (i.e. 350 μm and 254 mm^2), which presented an inverted pyramid-shaped microwell array, called reverse micromolding technique.

The structure, swelling ratio and electrical properties of calcium alginate were investigated, showing a network similar to a fishing net, with swelling ratio between 70 and 90 for low concentration of alginate and calcium solutions (respectively 10%, 15% and 20% w/V for alginate and 10mM for calcium solution). It was also demonstrated that calcium alginate has a very high ionic conductivity in the spheroids culture medium (DEME/F12, supplemented with FBS and P/S) and thus behave as an ion bridge.

The electrochemical response of the fabricated microelectrode array was investigated with and without the presence of the CA scaffold, as a way to determine the functionality of this device before applying it to cell cultures.

The MEA showed typical behaviour of electrochemical interfaces comprising an electrolyte and PEDOT:PSS, whose volumeric capacitance C/V was in agreement with values found in literature of ten of F/cm^2 [113]. In the thesis I conceived and demonstrated a a delamination of electrode, particularly for the smaller dimension (i.e. 50 μm), suggesting

that electrodes of 100 μm and 200 μm radii are more reliable and stable in prolonged test and successive measures.
The same tests were performed on the complete device, the h-MEA, to discern how the CA hydrogel could change the impedance and phase response of the MEA. As expected from the previous conductivity test, stable impedances or marginal increases (<10%) has been recorded with C/V comparable to ones obtained from the MEA. These last results turn out the feasibility of use of the h-MEA as an electrochemical sensor.
Finally, a study example of the h-MEA application for monitoring spheroids is presented. It was possible to record variations of phase and impedance in 4 different time after T98G cell lines seeding (at T=0h, T=10 min, T= 10 min and T= 4h). This cell type is of s great interest for concer studies and neuroscience research. It was observed a general increase in values of impedance as cells started to self-organise into a spheroid. The system was modelled with two RC element connected, one corresponding to the presence of cells and the other to the PEDOT:PSS.
All these results exposed reveal the successful fabrication of a biosensor able to register electrochemical responses and also able to detect spheroid formation, which take into account the necessities of such culture format, like cytotoxicity and control on spheroid dimension and disposition, given by the choice of materials used and dimension and disposition of the CA scaffold; while remaining still an open system to which other component could add to study their effects, such us radiation or drug effects.

Acknowledgements

The realisation of this thesis would not have been possible without the help and support given by several people that I have worked with.
First of all, I would like to thank my tutors, prof. Fraboni, prof. Schönherr, Dott. Zironi and Dott. De Cataldo, for giving me the opportunity to work at this project. I'd like also to thank prof. Cramer, who also played a crucial role in the development of this technology.
Thanks to this team I had an amazing and inspiring experience and I increased my researcher skills. Their guide and knowledge was fundamental to coordinate and carry on the several projects and experiments that I have done in this work.

Bibliography

[1] Xiaoqiu Dou, Ping Li, and Holger Schönherr. "Three-Dimensional Microstructured Poly(vinyl alcohol) Hydrogel Platform for the Controlled Formation of Multicellular Cell Spheroids". In: *Biomacromolecules* 19.1 (2018). PMID: 29161497, pp. 158–166. DOI: 10.1021/acs.biomac.7b01345. eprint: https://doi.org/10.1021/acs.biomac.7b01345. URL: https://doi.org/10.1021/acs.biomac.7b01345.

[2] Nelita T. Elliott and Fan Yuan. "A Review of Three-Dimensional In Vitro Tissue Models for Drug Discovery and Transport Studies". In: *Journal of Pharmaceutical Sciences* 100.1 (2011), pp. 59–74. ISSN: 0022-3549. DOI: https://doi.org/10.1002/jps.22257. URL: https://www.sciencedirect.com/science/article/pii/S0022354915323376.

[3] J Walker-Daniels and O Faklaris. "Live cell imaging methods review". In: *Mater Methods* 2 (2012), p. 124.

[4] Sverre Grimnes and Orjan G Martinsen. *Bioimpedance and bioelectricity basics*. Academic press, 2011.

[5] Alberto Yúfera Garcıa et al. "A Tissue Impedance Measurement Chip for Myocardial Ischemia Detection". In: *IEEE Transactions on Circuits and Systems I: Regular Papers, 52 (12), 2620-2628.* (2005).

[6] Stephen M Radke and Evangelyn C Alocilja. "Design and fabrication of a microimpedance biosensor for bacterial detection". In: *IEEE sensors journal* 4.4 (2004), pp. 434–440.

[7] Ivar Giaever and Charles R Keese. "Use of electric fields to monitor the dynamical aspect of cell behavior in tissue culture". In: *IEEE Transactions on Biomedical Engineering* 2 (1986), pp. 242–247.

[8] Ivar Giaever and Charles R Keese. "Micromotion of mammalian cells measured electrically." In: *Proceedings of the National Academy of Sciences* 88.17 (1991), pp. 7896–7900.

[9] Isaac O K'Owino and Omowunmi A Sadik. "Impedance spectroscopy: a powerful tool for rapid biomolecular screening and cell culture monitoring". In: *Electroanalysis: An International Journal Devoted to Fundamental and Practical Aspects of Electroanalysis* 17.23 (2005), pp. 2101–2113.

[10] Youchun Xu et al. "A review of impedance measurements of whole cells". In: *Biosensors and Bioelectronics* 77 (2016), pp. 824–836. ISSN: 0956-5663. DOI: https://doi.org/10.1016/j.bios.2015.10.027. URL: https://www.sciencedirect.com/science/article/pii/S0956566315304917.

[11] Sun-Mi Lee et al. "Real-time monitoring of 3D cell culture using a 3D capacitance biosensor". In: *Biosensors and Bioelectronics* 77 (2016), pp. 56–61.

[12] VF Curto et al. "A planar impedance sensor for 3D spheroids". In: *Lab on a Chip* 18.6 (2018), pp. 933–943.

[13] Sebastian C Bürgel et al. "Automated, multiplexed electrical impedance spectroscopy platform for continuous monitoring of microtissue spheroids". In: *Analytical chemistry* 88.22 (2016), pp. 10876–10883.

[14] Yuxiang Pan et al. "3D cell-based biosensor for cell viability and drug assessment by 3D electric cell/matrigel-substrate impedance sensing". In: *Biosensors and Bioelectronics* 130 (2019), pp. 344–351.

[15] Marco Carminati. "Advances in high-resolution microscale impedance sensors". In: *Journal of Sensors* 2017 (2017).

[16] Marco Carminati et al. "Impedance spectroscopy for biosensing: Circuits and applications". In: *Handbook of Biochips*. Springer, 2022, pp. 87–110.

[17] F Lisdat and D Schäfer. "The use of electrochemical impedance spectroscopy for biosensing". In: *Analytical and bioanalytical chemistry* 391.5 (2008), pp. 1555–1567.

[18] Hend S. Magar, Rabeay Y. A. Hassan, and Ashok Mulchandani. "Electrochemical Impedance Spectroscopy (EIS): Principles, Construction, and Biosensing Applications". In: *Sensors* 21.19 (2021). ISSN: 1424-8220. DOI: 10.3390/s21196578. URL: https://www.mdpi.com/1424-8220/21/19/6578.

[19] Koji Asami. "Characterization of biological cells by dielectric spectroscopy". In: *Journal of Non-Crystalline Solids* 305.1 (2002), pp. 268–277. ISSN: 0022-3093. DOI: https://doi.org/10.1016/S0022-3093(02)01110-9. URL: https://www.sciencedirect.com/science/article/pii/S0022309302011109.

[20] Kin Fong Lei, Tai-Kun Liu, and Ngan-Ming Tsang. "Towards a high throughput impedimetric screening of chemosensitivity of cancer cells suspended in hydrogel and cultured in a paper substrate". In: *Biosensors and Bioelectronics* 100 (2018), pp. 355–360. ISSN: 0956-5663. DOI: https://doi.org/10.1016/j.bios.2017.09.029. URL: https://www.sciencedirect.com/science/article/pii/S095656631730636X.

[21] Isabel del Agua et al. "Conducting Polymer Scaffolds Based on Poly(3,4-ethylenedioxythiophene) and Xanthan Gum for Live-Cell Monitoring". In: *ACS Omega* 3.7 (2018). PMID: 30087913, pp. 7424–7431. DOI: 10.1021/acsomega.8b00458. eprint: https://doi.org/10.1021/acsomega.8b00458. URL: https://doi.org/10.1021/acsomega.8b00458.

[22] Gokhan Bahcecioglu, Nesrin Hasirci, and Vasif Hasirci. "Cell behavior on the alginate-coated PLLA/PLGA scaffolds". In: *International Journal of Biological Macromolecules* 124 (2019), pp. 444–450. ISSN: 0141-8130. DOI: https://doi.org/10.1016/j.ijbiomac.2018.11.169. URL: https://www.sciencedirect.com/science/article/pii/S0141813018345252.

[23] Rukmani Sridharan et al. "Macrophage Polarization in Response to Collagen Scaffold Stiffness Is Dependent on Cross-Linking Agent Used To Modulate the Stiffness". In: *ACS Biomaterials Science & Engineering* 5.2 (2019). PMID: 33405818, pp. 544–552. DOI: 10.1021/acsbiomaterials.8b00910. eprint: https://doi.org/10.1021/acsbiomaterials.8b00910. URL: https://doi.org/10.1021/acsbiomaterials.8b00910.

[24] F Groeber et al. "Impedance spectroscopy for the non-destructive evaluation of in vitro epidermal models". In: *Pharmaceutical research* 32.5 (2015), pp. 1845–1854. DOI: 10.1007/s11095-014-1580-3.

[25] Ole William Petersen et al. "Interaction with basement membrane serves to rapidly distinguish growth and differentiation pattern of normal and malignant human breast epithelial cells." In: *Proceedings of the National Academy of Sciences* 89.19 (1992), pp. 9064–9068.

[26] Steven R Caliari and Jason A Burdick. "A practical guide to hydrogels for cell culture". In: *Nature methods* 13.5 (2016), pp. 405–414.

[27] Mark W. Tibbitt and Kristi S. Anseth. "Hydrogels as extracellular matrix mimics for 3D cell culture". In: *Biotechnology and Bioengineering* 103.4 (2009), pp. 655–663. DOI: https://doi.org/10.1002/bit.22361. eprint: https://onlinelibrary.wiley.com/doi/pdf/10.1002/bit.22361. URL: https://onlinelibrary.wiley.com/doi/abs/10.1002/bit.22361.

[28] Kytai Truong Nguyen and Jennifer L West. "Photopolymerizable hydrogels for tissue engineering applications". In: *Biomaterials* 23.22 (2002), pp. 4307–4314.

[29] Ruth R Chen and David J Mooney. "Polymeric growth factor delivery strategies for tissue engineering". In: *Pharmaceutical research* 20.8 (2003), pp. 1103–1112.

[30] Anna Birgersdotter, Rickard Sandberg, and Ingemar Ernberg. "Gene expression perturbation in vitro—a growing case for three-dimensional (3D) culture systems". In: *Seminars in cancer biology*. Vol. 15. 5. Elsevier. 2005, pp. 405–412.

[31] MP Lutolf and JA Hubbell. "Synthetic biomaterials as instructive extracellular microenvironments for morphogenesis in tissue engineering". In: *Nature biotechnology* 23.1 (2005), pp. 47–55.

[32] Ana H Bacelar et al. ""Smart" hydrogels in tissue engineering and regenerative medicine applications". In: *Handbook of intelligent scaffolds for tissue engineering and regenerative medicine*. Jenny Stanford Publishing, 2017, pp. 333–367.

[33] Jonathan T Butcher and Robert M Nerem. "Porcine aortic valve interstitial cells in three-dimensional culture: comparison of phenotype with aortic smooth muscle cells". In: *Journal of Heart Valve Disease* 13.3 (2004), pp. 478–486.

[34] Daniela Eyrich et al. "Long-term stable fibrin gels for cartilage engineering". In: *Biomaterials* 28.1 (2007), pp. 55–65.

[35] Kristyn S Masters et al. "Designing scaffolds for valvular interstitial cells: cell adhesion and function on naturally derived materials". In: *Journal of Biomedical Materials Research Part A: An Official Journal of The Society for Biomaterials, The Japanese Society for Biomaterials, and The Australian Society for Biomaterials and the Korean Society for Biomaterials* 71.1 (2004), pp. 172–180.

[36] Abdel Kareem Azab et al. "Crosslinked chitosan implants as potential degradable devices for brachytherapy: in vitro and in vivo analysis". In: *Journal of controlled release* 111.3 (2006), pp. 281–289.

[37] JE Barralet et al. "Comparison of bone marrow cell growth on 2D and 3D alginate hydrogels". In: *Journal of materials science: materials in medicine* 16.6 (2005), pp. 515–519.

[38] Eileen Dawson et al. "Biomaterials for stem cell differentiation". In: *Advanced drug delivery reviews* 60.2 (2008), pp. 215–228.

[39] Amarpreet S Sawhney, Chandrashekhar P Pathak, and Jeffrey A Hubbell. "Bioerodible hydrogels based on photopolymerized poly (ethylene glycol)-co-poly (. alpha.-hydroxy acid) diacrylate macromers". In: *Macromolecules* 26.4 (1993), pp. 581–587.

[40] AT Metters, KS Anseth, and CN Bowman. "Fundamental studies of a novel, biodegradable PEG-b-PLA hydrogel". In: *Polymer* 41.11 (2000), pp. 3993–4004.

[41] Traian V Chirila et al. “Poly (2-hydroxyethyl methacrylate) sponges as implant materials: in vivo and in vitro evaluation of cellular invasion”. In: *Biomaterials* 14.1 (1993), pp. 26–38.

[42] Chunguang Zhang et al. “Preparation of alginate oligosaccharides and their biological activities in plants: A review”. In: *Carbohydrate Research* 494 (2020), p. 108056.

[43] Adam Saltz and Umadevi Kandalam. “Mesenchymal stem cells and alginate microcarriers for craniofacial bone tissue engineering: A review”. In: *Journal of biomedical materials research Part A* 104.5 (2016), pp. 1276–1284.

[44] Aurora C Hernández-González, Lucıa Téllez-Jurado, and Luis M Rodrıguez-Lorenzo. “Alginate hydrogels for bone tissue engineering, from injectables to bioprinting: A review”. In: *Carbohydrate polymers* 229 (2020), p. 115514.

[45] Nguyen Thi Thanh Uyen et al. “Fabrication of alginate microspheres for drug delivery: A review”. In: *International journal of biological macromolecules* 153 (2020), pp. 1035–1046.

[46] Nanna Rhein-Knudsen et al. “Characterization of alginates from Ghanaian brown seaweeds: Sargassum spp. and Padina spp.” In: *Food Hydrocolloids* 71 (2017), pp. 236–244.

[47] Xi Guo et al. “Structures, properties and application of alginic acid: A review”. In: *International Journal of Biological Macromolecules* 162 (2020), pp. 618–628.

[48] Marta Szekalska et al. “Alginate: current use and future perspectives in pharmaceutical and biomedical applications”. In: *International Journal of Polymer Science* 2016 (2016).

[49] Hengtong Zhang, Junqiu Cheng, and Qiang Ao. “Preparation of Alginate-Based Biomaterials and Their Applications in Biomedicine”. In: *Marine Drugs* 19.5 (2021). ISSN: 1660-3397. DOI: 10.3390/md19050264. URL: https://www.mdpi.com/1660-3397/19/5/264.

[50] Therese Andersen, Pia Auk-Emblem, and Michael Dornish. “3D cell culture in alginate hydrogels”. In: *Microarrays* 4.2 (2015), pp. 133–161.

[51] Ivan Donati et al. “New hypothesis on the role of alternating sequences in calcium-alginate gels”. In: *Biomacromolecules* 6.2 (2005), pp. 1031–1040.

[52] Liangbin Li et al. “Reexamining the egg-box model in calcium- alginate gels with X-ray diffraction”. In: *Biomacromolecules* 8.2 (2007), pp. 464–468.

[53] Olav Smidsrd. “Some physical properties of alginates in solution and in the gel state”. In: (1973).

[54] B Allison Harper et al. “Effect of various gelling cations on the physical properties of “wet” alginate films”. In: *Journal of food science* 79.4 (2014), E562–E567.

[55] BE Christensen. "Alginates as biomaterials in tissue engineering". In: *Carbohydrate chemistry: chemical and biological approaches* 37 (2011), pp. 227–258.

[56] Kuen Yong Lee, Kamal H Bouhadir, and David J Mooney. "Controlled degradation of hydrogels using multi-functional cross-linking molecules". In: *Biomaterials* 25.13 (2004), pp. 2461–2466.

[57] Buddy D Ratner et al. "Biomaterials science: an introduction to materials in medicine". In: *San Diego, California* (2004), pp. 162–4.

[58] Michelle A LeRoux, Farshid Guilak, and Lori A Setton. "Compressive and shear properties of alginate gel: effects of sodium ions and alginate concentration". In: *Journal of Biomedical Materials Research: An Official Journal of The Society for Biomaterials, The Japanese Society for Biomaterials, and The Australian Society for Biomaterials and the Korean Society for Biomaterials* 47.1 (1999), pp. 46–53.

[59] Catherine K Kuo and Peter X Ma. "Ionically crosslinked alginate hydrogels as scaffolds for tissue engineering: Part 1. Structure, gelation rate and mechanical properties". In: *Biomaterials* 22.6 (2001), pp. 511–521.

[60] Jeanie L Drury, Robert G Dennis, and David J Mooney. "The tensile properties of alginate hydrogels". In: *Biomaterials* 25.16 (2004), pp. 3187–3199.

[61] Ashutosh Agarwal et al. "Micropatterning alginate substrates for in vitro cardiovascular muscle on a chip". In: *Advanced functional materials* 23.30 (2013), pp. 3738–3746.

[62] AB Lansdown and MJ Payne. "An evaluation of the local reaction and biodegradation of calcium sodium alginate (Kaltostat) following subcutaneous implantation in the rat." In: *Journal of the Royal College of Surgeons of Edinburgh* 39.5 (1994), pp. 284–288.

[63] Hyun Joon Kong et al. "Controlling degradation of hydrogels via the size of crosslinked junctions". In: *Advanced materials* 16.21 (2004), pp. 1917–1921.

[64] Alexander D Augst, Hyun Joon Kong, and David J Mooney. "Alginate hydrogels as biomaterials". In: *Macromolecular bioscience* 6.8 (2006), pp. 623–633.

[65] Jon A Rowley, Gerard Madlambayan, and David J Mooney. "Alginate hydrogels as synthetic extracellular matrix materials". In: *Biomaterials* 20.1 (1999), pp. 45–53.

[66] Masaya Yamamoto et al. "Generation of stable co-cultures of vascular cells in a honeycomb alginate scaffold". In: *Tissue Engineering Part A* 16.1 (2010), pp. 299–308.

[67] Yulia Sapir et al. "The promotion of in vitro vessel-like organization of endothelial cells in magnetically responsive alginate scaffolds". In: *Biomaterials* 33.16 (2012), pp. 4100–4109.

[68] Marita Westhrin et al. "Osteogenic differentiation of human mesenchymal stem cells in mineralized alginate matrices". In: *PloS one* 10.3 (2015), e0120374.

[69] Sarah Roxana Herlofsen et al. "Chondrogenic differentiation of human bone marrow-derived mesenchymal stem cells in self-gelling alginate discs reveals novel chondrogenic signature gene clusters". In: *Tissue Engineering Part A* 17.7-8 (2011), pp. 1003–1013.

[70] Jinah Jang et al. "Effects of alginate hydrogel cross-linking density on mechanical and biological behaviors for tissue engineering". In: *Journal of the Mechanical Behavior of Biomedical Materials* 37 (2014), pp. 69–77.

[71] E Alsberg et al. "Cell-interactive alginate hydrogels for bone tissue engineering". In: *Journal of dental research* 80.11 (2001), pp. 2025–2029.

[72] Sean V Murphy and Anthony Atala. "3D bioprinting of tissues and organs". In: *Nature biotechnology* 32.8 (2014), pp. 773–785.

[73] Saif Khalil and Wei Sun. "Bioprinting endothelial cells with alginate for 3D tissue constructs". In: *Journal of biomechanical engineering* 131.11 (2009).

[74] Meik Neufurth et al. "Engineering a morphogenetically active hydrogel for bioprinting of bioartificial tissue derived from human osteoblast-like SaOS-2 cells". In: *Biomaterials* 35.31 (2014), pp. 8810–8819.

[75] Xiaohong Wang et al. "Effect of bioglass on growth and biomineralization of SaOS-2 cells in hydrogel after 3D cell bioprinting". In: *PLoS One* 9.11 (2014), e112497.

[76] Yu Zhao et al. "Three-dimensional printing of Hela cells for cervical tumor model in vitro". In: *Biofabrication* 6.3 (2014), p. 035001.

[77] Jia Jia et al. "Engineering alginate as bioink for bioprinting". In: *Acta biomaterialia* 10.10 (2014), pp. 4323–4331.

[78] Sahika Inal et al. "Conjugated Polymers in Bioelectronics". In: *Accounts of Chemical Research* 51.6 (2018), pp. 1368–1376. DOI: 10.1021/acs.accounts.7b00624. eprint: https://doi.org/10.1021/acs.accounts.7b00624. URL: https://doi.org/10.1021/acs.accounts.7b00624.

[79] Andreas Elschner et al. *PEDOT: principles and applications of an intrinsically conductive polymer*. CRC press, 2010.

[80] J.R. Reynolds et al. "Unique variable-gap polyheterocycles for high-contrast dual polymer electrochromic devices". In: *Synthetic Metals* 85.1 (1997), pp. 1295–1298. ISSN: 0379-6779. DOI: https://doi.org/10.1016/S0379-6779(97)80248-2. URL: https://www.sciencedirect.com/science/article/pii/S0379677997802482.

[81] Y Wang. "Research progress on a novel conductive polymer–poly(3,4-ethylenedioxythiophene) (PEDOT)". In: *Journal of Physics: Conference Series* 152.1 (Mar. 2009), p. 012023. DOI: 10.1088/1742-6596/152/1/012023. URL: https://dx.doi.org/10.1088/1742-6596/152/1/012023.

[82] Michael Dietrich et al. "Electrochemical and spectroscopic characterization of polyalkylenedioxythiophenes". In: *Journal of Electroanalytical Chemistry* 369.1-2 (1994), pp. 87–92.

[83] C Kvarnström et al. "In situ FTIR spectroelectrochemical characterization of poly (3, 4-ethylenedioxythiophene) films". In: *Synthetic metals* 101.1-3 (1999), p. 66.

[84] Stephan Kirchmeyer and Knud Reuter. "Scientific importance, properties and growing applications of poly (3, 4-ethylenedioxythiophene)". In: *Journal of Materials Chemistry* 15.21 (2005), pp. 2077–2088.

[85] Jonathan Rivnay et al. "Structural control of mixed ionic and electronic transport in conducting polymers". In: *Nature communications* 7.1 (2016), pp. 1–9.

[86] K Jeuris et al. "Light stability of 3, 4-ethylenedioxythiophene-based derivatives". In: *Synthetic metals* 132.3 (2003), pp. 289–295.

[87] Udo Lang, Nicola Naujoks, and Jurg Dual. "Mechanical characterization of PEDOT: PSS thin films". In: *Synthetic Metals* 159.5-6 (2009), pp. 473–479.

[88] AN Aleshin, SR Williams, and AJ Heeger. "Transport properties of poly (3, 4-ethylenedioxythiophene)/poly (styrenesulfonate)". In: *Synthetic Metals* 94.2 (1998), pp. 173–177.

[89] G Greczynski et al. "Photoelectron spectroscopy of thin films of PEDOT–PSS conjugated polymer blend: a mini-review and some new results". In: *Journal of Electron Spectroscopy and Related Phenomena* 121.1 (2001). Electron Spectroscopy of polymer surfaces, pp. 1–17. ISSN: 0368-2048. DOI: https://doi.org/10.1016/S0368-2048(01)00323-1. URL: https://www.sciencedirect.com/science/article/pii/S0368204801003231.

[90] Alexandre Mantovani Nardes et al. "Microscopic understanding of the anisotropic conductivity of PEDOT: PSS thin films". In: *Advanced Materials* 19.9 (2007), pp. 1196–1200.

[91] Alexandre Mantovani Nardes, Rene AJ Janssen, and Martijn Kemerink. "A morphological model for the solvent-enhanced conductivity of PEDOT: PSS thin films". In: *Advanced Functional Materials* 18.6 (2008), pp. 865–871.

[92] Jianyong Ouyang et al. "On the mechanism of conductivity enhancement in poly (3, 4-ethylenedioxythiophene): poly (styrene sulfonate) film through solvent treatment". In: *Polymer* 45.25 (2004), pp. 8443–8450.

[93] Nevill Francis Mott and Edward A Davis. *Electronic processes in non-crystalline materials*. Oxford university press, 2012.

[94] Lorenzo Margotti. "On the fabrication of a synthetic voltage-gated ion channel based on organic mixed ion-electron conductors". Msc thesis. University of Bologna, 2021.

[95] Nicholas A Geisse. "AFM and combined optical techniques". In: *Materials today* 12.7-8 (2009), pp. 40–45.

[96] Dalia G Yablon. "Overview of atomic force microscopy". In: *Scanning Probe Microscopy in Industrial Applications: Nanomechanical Characterization* (2013), pp. 1–14.

[97] Peter EJ Flewitt and Robert K Wild. *Physical methods for materials characterisation*. CRC Press, 2017. Chap. 6.

[98] Gretchen H Stein. "T98G: An anchorage-independent human tumor cell line that exhibits stationary phase G1 arrest in vitro". In: *Journal of cellular physiology* 99.1 (1979), pp. 43–54.

[99] Mariam-Eleni Oraiopoulou et al. "A 3D tumor spheroid model for the T98G Glioblastoma cell line phenotypic characterization". In: *Tissue and Cell* 59 (2019), pp. 39–43.

[100] Hyun Joon Kong, Kuen Yong Lee, and David J Mooney. "Nondestructively probing the cross-linking density of polymeric hydrogels". In: *Macromolecules* 36.20 (2003), pp. 7887–7890.

[101] A Martinsen, G Skjåk-Bræk, and O Smidsrød. "Alginate as immobilization material: I. Correlation between chemical and physical properties of alginate gel beads". In: *Biotechnology and bioengineering* 33.1 (1989), pp. 79–89.

[102] Stéphane Roger, Delphine Talbot, and Agnes Bee. "Preparation and effect of Ca2+ on water solubility, particle release and swelling properties of magnetic alginate films". In: *Journal of Magnetism and Magnetic Materials* 305.1 (2006), pp. 221–227.

[103] Kurt Ingar Draget et al. "Effects of molecular weight and elastic segment flexibility on syneresis in Ca-alginate gels". In: *Food Hydrocolloids* 15.4-6 (2001), pp. 485–490.

[104] Maya Davidovich-Pinhas and Havazelet Bianco-Peled. "A quantitative analysis of alginate swelling". In: *Carbohydrate Polymers* 79.4 (2010), pp. 1020–1027.

[105] Paul J Flory. "Network Structure and the Elastic Properties of Vulcanized Rubber." In: *Chemical reviews* 35.1 (1944), pp. 51–75.

[106] Hong Wu et al. "Molecularly imprinted organic–inorganic hybrid membranes for selective separation of phenylalanine isomers and its analogue". In: *Separation and purification technology* 68.1 (2009), pp. 97–104.

[107] Fumio Kurayama et al. “Facile preparation of aminosilane-alginate hybrid beads for enzyme immobilization: kinetics and equilibrium studies”. In: *International journal of biological macromolecules* 150 (2020), pp. 1203–1212.

[108] Fumio Kurayama et al. “Preparation of aminosilane–alginate hybrid microcapsules and their use for enzyme encapsulation”. In: *Journal of Materials Chemistry* 22.30 (2012), pp. 15405–15411.

[109] Qi Lang et al. “AC Electrothermal Circulatory Pumping Chip for Cell Culture”. In: *ACS applied materials interfaces* 7 (Nov. 2015). DOI: 10.1021/acsami.5b08863.

[110] Rossana Di Martino et al. “Analysis of the role of elution buffers on the separation capabilities of dielectrophoretic devices”. In: *Sensing and Bio-Sensing Research* 7 (2016), pp. 162–167. ISSN: 2214-1804. DOI: https://doi.org/10.1016/j.sbsr.2015.12.001. URL: https://www.sciencedirect.com/science/article/pii/S2214180415300404.

[111] Xinyan Tracy Cui and David Daomin Zhou. “Poly (3, 4-ethylenedioxythiophene) for chronic neural stimulation”. In: *IEEE Transactions on Neural Systems and Rehabilitation Engineering* 15.4 (2007), pp. 502–508.

[112] Maria Vomero et al. “Highly stable glassy carbon interfaces for long-term neural stimulation and low-noise recording of brain activity”. In: *Scientific reports* 7.1 (2017), pp. 1–14.

[113] Anton V Volkov et al. “Understanding the capacitance of PEDOT: PSS”. In: *Advanced Functional Materials* 27.28 (2017), p. 1700329.

[114] Tom Elsdale and Jonathan Bard. “Collagen substrata for studies on cell behavior”. In: *The Journal of cell biology* 54.3 (1972), pp. 626–637.